

Article

Comparison of Separation Control Mechanisms for Synthetic Jet and Plasma Actuators

Yoshiaki Abe ^{1,*}, Taku Nonomura ², Makoto Sato ³, Hikaru Aono ⁴ and Kozo Fujii ⁵¹ Department of Aeronautics and Astronautics, The University of Tokyo, Yokohama 252-5210, Japan² Department of Aerospace Engineering, Tohoku University, Sendai 980-8579, Japan; nonomura@tohoku.ac.jp³ Department of Mechanical Science and Engineering, Kogakuin University, Tokyo 163-8677, Japan; msato@cc.kogakuin.ac.jp⁴ Department of Mechanical Engineering and Robotics, Shinshu University, Nagano 386-8567, Japan; aono@shinshu-u.ac.jp⁵ Department of Information and Computer Technology, Tokyo University of Science, Tokyo 125-8585, Japan; fujii@rs.tus.ac.jp

* Correspondence: yoshiaki.abe@tohoku.ac.jp

† Current address: Institute of Fluid Science, Tohoku University, Sendai 980-8577, Japan.

Abstract: This study numerically investigated the mechanisms of separation control using a synthetic jet (SJ) and plasma actuator (PA) around an NACA0015 airfoil at the chord Reynolds number of 63,000. Both SJ and PA were installed on the leading edge with the same order of input momentum ($C_\mu = O(10^{-3}-10^{-5})$) and the same actuation frequencies in $F^+ = 1.0-30$. The momentum coefficient C_μ is defined as the normalized momentum introduced from the SJ or the PA, and F^+ stands for the actuation frequency normalized by the chord length and uniform velocity. A number of large-eddy simulations (LES) were conducted for the SJ and the PA, and the mechanisms were clarified in terms of the exchange of chordwise momentum with Reynolds shear stress and coherent vortex structures. First, four main differences in the induced flows of the SJ and the PA were clarified as follows: (A) wall-tangential velocity; (B) three-dimensional flow structures; (C) spatial locality; and (D) temporal fluctuation. Then, a common feature of flow control by the SJ and the PA was revealed: a lift-to-drag ratio was found to be better recovered in $F^+ = 6.0-20$ than in other frequencies. Although there were differences in the induced flows, the phase decomposition of the flow fields identified common mechanisms that the turbulent component of the Reynolds shear stress mainly contributes to the exchange of the chordwise (streamwise) momentum; and the turbulent vortices are convected over the airfoil surface by the coherent spanwise vortices in the frequency of F^+ .

Keywords: flow control; separation control; synthetic jet; plasma actuator; CFD; LES

Citation: Abe, Y.; Nonomura, T.; Sato, M.; Aono, H.; Fujii, K. Comparison of Separation Control Mechanisms for Synthetic Jet and Plasma Actuators. *Actuators* **2023**, *12*, 322. <https://doi.org/10.3390/act12080322>

Academic Editor: Subrata Roy

Received: 4 May 2023

Revised: 4 August 2023

Accepted: 7 August 2023

Published: 11 August 2023



Copyright: © 2023 by the authors. Licensee MDPI, Basel, Switzerland. This article is an open access article distributed under the terms and conditions of the Creative Commons Attribution (CC BY) license (<https://creativecommons.org/licenses/by/4.0/>).

1. Introduction

An improvement of the capability to suppress flow separation brings a great benefit to systems which have fluid flow in or around them. The typical and conventional devices for separation control are a mechanical “flap” and “slat” implemented on aircraft wings, which, however, require complicated systems and result in increasing the structural weight. To replace these conventional devices, “microdevices” that are simple, small, and have low energy consumption have been investigated by many researchers [1–3].

This study focuses on the separation control at low-Reynolds-number ($Re = O(10^4)$) flows around the airfoil and the use of two active-control devices: a synthetic jet (SJ) and a plasma actuator (PA). The SJ, also known as a zero-net-mass-flux jet, consists of a cavity and an orifice connected to the cavity, of which the bottom oscillates with a small amplitude, and produces a weak and periodic flow from the orifice exit. The PA generates plasma to put kinetic energy inside the boundary layer by means of direct current, alternative current, radio frequency (RF), microwave, arc, corona, and spark electric discharge. Both SJ [4–10]

and PA [11–15] are categorized as microdevices, which are small ($O(10)$ mm), light-weight, and are more simple and have lower energy consumption than conventional devices.

Based on the recent studies, one of the key phenomena in the effective control at a low-Reynolds-number regime has been clarified to be an unsteadiness of input disturbance and the excitation of shear layer instabilities [9,10,13,15–17]. Most of those attempts to investigate the separation control mechanism for those microdevices can be seen for each device independently. Specifically, the separation control by the SJ was investigated in [9,10], and that by the PA was performed in [13,15–17]. However, few researchers have tried to compare either the capabilities or mechanisms of separation control between different devices, which cannot lead to the development of basic and general design criteria for the separation control. This paper focuses on the quasi-steady state of the controlled flow fields with the SJ and the PA, while the transient phase from separated to attached flows is similarly significant for control capability. The latter transient mechanism will be targeted in a future study.

Extensive studies on the SJ have been performed experimentally [4,6]. Smith and Glezer investigated basic characteristics of induced flows by the SJ. Later, [5] experimentally revealed that the induced flow is initially a pair of vortices that is transient to a turbulent jet as evolving in the vertical direction. On the other hand, [18] performed a Reynolds-averaged Navier–Stokes simulation (RANS), which agrees well with the experimental results in the time-averaged vertical velocity; however, the other turbulent statistics such as velocity fluctuations were not in good agreement. This is probably due to the use of the RANS that often fails to capture unsteady turbulent statistics and the computational model of the SJ that adopts a boundary condition of a top-hat velocity distribution on the airfoil surface, where the flow inside the cavity was not resolved. Okada et al. [8] conducted a large-eddy simulation (LES) resolving the flows inside the orifice and cavity, where the velocity fluctuation qualitatively agrees well with the experimental results. Therefore, both a high-fidelity model of the SJ and the unsteady flow simulation, e.g., LES, are necessary for an accurate prediction of the induced flows by the SJ. The present study follows [8] for the modeling of the SJ using the orifice and deforming cavity with a uniform shape in the spanwise direction. For the actuation frequency, which is one of the most significant parameters for control, most of the previous studies reported that the low-frequency control utilizes the wake instability [7,9,19]. Meanwhile, although the actuator is not limited to the SJ, it has been shown that the high-frequency control utilizes several flow phenomena, including the shear layer instability [20,21] and turbulent transition/mixing enhancement [13]. The advantage of high-frequency control for dynamic stall on a pitching airfoil was also demonstrated experimentally and numerically [22,23].

Meanwhile, studies on the PA have also been conducted. Asada and Fujii [24] investigated the capabilities and control mechanisms of the burst mode actuation around a NACA0015 airfoil through a large-eddy simulation, where the $F^+ = 6.0$ actuation achieves better aerodynamic performance than $F^+ = 1.0$. They also reported that the difference is mainly caused by the promotion of a turbulent transition on a laminar-separated bubble [24]. Subsequently, Sato et al. [13,15] more precisely clarified the mechanism of the effective control using the burst mode through the numerical analysis of Reynolds stress decomposition and linear stability theory (LST) [13]. More recently, Yarusevych et al. [25,26] performed an experimental study for the steady and transient response of a laminar separation bubble (LSB) using the PA. They employed the LST analysis to relate the shear layer stability and the bubble dynamics. In the LSB, the unstable disturbances in the separated shear layer is amplified and roll-up vortices are formed from the shear layer by the flow control. Those roll-up vortices are locked onto a excitation frequency with a strong coherent structure if the excitation frequency is sufficiently close to the unstable frequency. The spatial growth of disturbance and the coherent vortex structures were also reported in [27,28]. An extensive experimental study on the separation control using the PA was performed by Sekimoto et al. [29], and they classified the control trends based on the separation conditions such as leading-edge and trailing-edge separation.

Thus far, the separation control capabilities and mechanisms of those microdevices have been extensively investigated numerically and experimentally. Both SJ and PA introduce spatially and temporally localized flows, although they have different operation mechanisms in the generation of disturbance. Therefore, a similarity is expected to exist behind the separation-control mechanisms using the SJ and the PA, which has not been rigorously investigated. The objective of this study is to clarify a common mechanism for separation control around the airfoil using the SJ and the PA. The flow field was assumed to be in the low-Reynolds-number regime ($Re = 63,000$) around the NACA0015 airfoil, and the LES was conducted to compare the separation control using the SJ and the PA. The difference in the input disturbance as well as the mechanisms to maintain the suppression of the separated flow were compared in detail.

The remainder of the paper is organized as follows. Section 2 specifies the problem settings and numerical models for the SJ and the PA. Section 3 describes the numerical methods. Section 4.1 discusses the flows induced by the PA and the SJ and compares the differences. Then, in Section 4.2, the separation-control capabilities are arranged from the viewpoint of the effect of F^+ for both devices, and the characteristics common for each device are clarified. Finally, Section 5 concludes the present study.

2. Problem Specifications

2.1. Separated Flow

This study focuses on the separation control around the NACA0015 airfoil at the chord Reynolds number of 63,000. The angle of attack was set to be 12° , wherein the flow is separated near the leading edge, i.e., approximately 2.0% of the chord length from the leading edge [24]. Such a flow condition helps us clarify the mechanism of amplification of extremely small disturbances from the SJ or the PA and resultant modification of the entire flows. For ease of comparison, the specific chord length and the inflow velocity are introduced herein: for example, the chord length $c_h = 0.1$ m and inflow air velocity $u_\infty = 10.0$ m/s correspond to the Reynolds number of 63,000. The experimental condition above was used for the validation study in [10,13,24].

2.2. Configuration of the SJ

A two-dimensional shape along the span was adopted for the orifice and cavity of the SJ for simplicity, as shown in Figure 1. The SJ was installed on the leading edge of the airfoil, and its orifice was normal to the airfoil surface. Figure 1b shows the details of the SJ, where green and blue colored regions indicate an airfoil surface and the SJ, respectively. The bottom of the cavity oscillates periodically and the flow inside the cavity and orifice was numerically solved. The orifice width l_e was set to be 0.5% of the chord length ($l_e = 0.005c_h$, where c_h is the chord length), which was often used in previous studies [8,30]. The orifice height was set to be l_e ; the cavity depth is denoted by $L(t)$ (t is the nondimensional time), which was initially set as $L(0) = L_0 = 10l_e$; and the width of the cavity bottom was set as $l_b = 5.5l_e$. The nondimensional value of actuation frequency f is denoted by F^+ according to the previous studies [1,8]. F^+ is defined as

$$F^+ = \frac{f^* c_h}{u_\infty}, \quad (1)$$

which is the same normalization as the Strouhal number, St , based on the same reference length and velocity. It should be noticed that although the normalization of F^+ is the same as St , they are distinguished in this paper, since F^+ is imposed as a controllable parameter unlike naturally excited frequencies in the flow. The bottom of the cavity oscillates in a translational motion according to Equation (2). The amplitude of oscillation is denoted by A (normalized by c_h), and the cavity depth $L(t)$ is defined as follows:

$$L(t) = L_0 + A \cos(2\pi F^+ t). \quad (2)$$

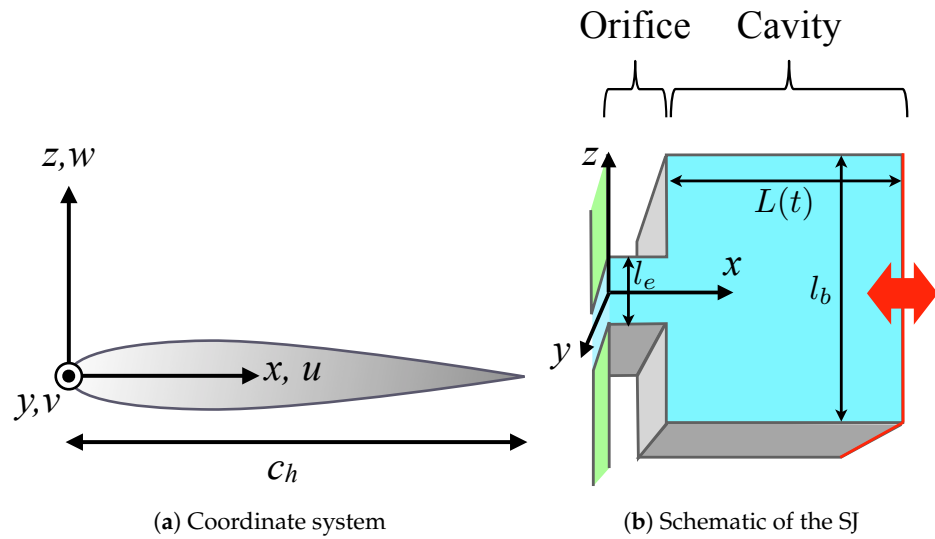


Figure 1. Coordinate system and geometrical configurations of the SJ.

Figure 2 shows the schematic diagram of the time history of the cavity depth $L(t)$. The momentum coefficient C_μ is defined by Equation (3), which is the ratio of the momentum induced by the SJ and the freestream per unit time. This definition assumes the incompressible fluid, and the maximum momentum (ρu_{\max}) induced by the SJ is approximately estimated as follows:

$$C_\mu = \frac{\rho u_{\max}^2 l_e}{\rho u_\infty^2 c_h}, \quad u_{\max} l_e = l_b \max\left(\frac{dL(t)}{dt}\right) = 2\pi l_b A F^+ \tag{3}$$

Note that the amplitude A is changed according to F^+ when C_μ is kept constant as $A = u_\infty \sqrt{c_h C_\mu l_b} / (2\pi F^+ l_e)$.

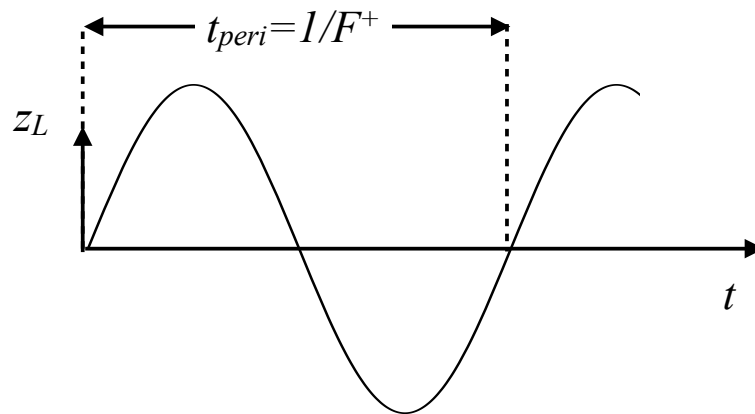


Figure 2. Schematic diagram of the time history of the cavity depth in the SJ, where t_{peri} is the period of the oscillation.

2.3. Configuration of the PA

The PA consists of two electrodes and a dielectric, of which the schematics are illustrated in Figure 3a. A high AC voltage generates plasma in between two electrodes, which induces a flow over the PA. The base frequency of AC voltage is denoted as f_{base} hereinafter, which is approximately 60Hz in the experiment. The burst mode actuation is defined by the multiplication of a sinusoidal higher base frequency and the lower frequency of the square wave (i.e., a step function) in the temporal direction, where the on and off phases are periodically enforced to input voltage in addition to the base-frequency oscillation

(see Figure 3c) [31]. The lower frequency of the square wave is called a “burst frequency” in the previous studies, i.e., f . The burst frequency f is normalized to F^+ according to Equation (1) based on the same definition as that used for the actuation frequency of the SJ. F^+ is called the actuation frequency for the conciseness of the notation throughout this paper.

The details of the settings and series of verification studies for the present PA model can be referred to in Sato et al. [13] and Aono et al. [32]. The details of the PA model is described as follows. The PA was modeled by the unsteady body force and energy based on the Suzen model [33], which has a spanwise-uniform (two-dimensional) distribution. Based on this modeling, source terms were added to the momentum and energy equations of the compressible Navier–Stokes equations. Precisely, the body force term is expressed as $D_c \mathbf{S}$ and the energy term is $D_c \mathbf{S} \cdot \mathbf{u}$. The nondimensional parameter D_c denotes the ratio of the energy input from the PA and a dynamic pressure of the freestream as follows:

$$D_c = \frac{Q_{c,\text{ref}} E_{\text{ref}} c_h}{\rho_\infty u_\infty^2}, \quad (4)$$

where $Q_{c,\text{ref}}$ and E_{ref} were given by the spatially maximum values of Q_c (electric charge) and $|E|$ (magnitude of an electric field) preliminary computed by the Suzen model [33], that is, a physical model of the PA. $\mathbf{S} = (S_x, S_y, S_z)$ denotes the body force vector, which was computed by $\mathbf{S} = Q\mathbf{E}/Q_{c,\text{ref}}E_{\text{ref}}$. Figure 3b illustrates the computational result of the Suzen model [13,32], where the component of the body force in the x direction (S_x) is shown. The grey and red regions indicate the wall and the exposed electrode, respectively. This study focuses on the PA implemented at the leading edge of the airfoil. Therefore, the actual body force distribution used in the computation was that rotated in the clockwise direction by 90° . Namely, the horizontal axis in Figure 3b, denoted as x , was in the tangential direction of the airfoil surface. The original Suzen model only defined the steady distribution and thus the unsteady model was introduced as follows:

$$\mathbf{S} = \mathbf{S}_{\text{suzen}} \sin^2(2\pi F_{\text{base}} t), \quad (5)$$

where the base frequency of AC voltage f_{base} is normalized by the chord length and freestream velocity as

$$F_{\text{base}} = \frac{f_{\text{base}} c_h}{u_\infty}. \quad (6)$$

The burst ratio BR was introduced as $BR = t_{\text{on}}/t_{\text{peri}}$, and the time history of the input voltage including the burst mode is illustrated in Figure 3c. The present unsteady model was sufficiently validated through the comparison with experiments by Aono et al. [32]. The governing equations for the flow are the compressible Navier–Stokes equations. The present PA model is implemented into the momentum and energy equations as follows:

$$\frac{\partial \rho}{\partial t} + \frac{\partial \rho u_k}{\partial x_k} = 0, \quad (7)$$

$$\frac{\partial \rho u_i}{\partial t} + \frac{\partial (\rho u_i u_k + p \delta_{ik})}{\partial x_k} = \frac{1}{Re} \frac{\partial \tau_{ik}}{\partial x_k} + D_c S_i, \quad (8)$$

$$\frac{\partial e}{\partial t} + \frac{\partial ((e + p) u_k)}{\partial x_k} = \frac{1}{Re} \frac{\partial u_l \tau_{kl}}{\partial x_k} + \frac{1}{(\gamma - 1) Pr Re Ma^2} \frac{\partial q_k}{\partial x_k} + D_c S_k u_k, \quad (9)$$

where x_i , u_i , q_i , ρ , p , e , τ_{ij} , δ_{ij} , and t denote the nondimensional forms of position vector, velocity vector, heat flux vector, density, pressure, energy per unit volume, stress tensor, Kronecker delta, and time, respectively. Note that S_i denotes the component of \mathbf{S} defined in Equation (5). The Einstein summation convention is used in Equations (7)–(9).

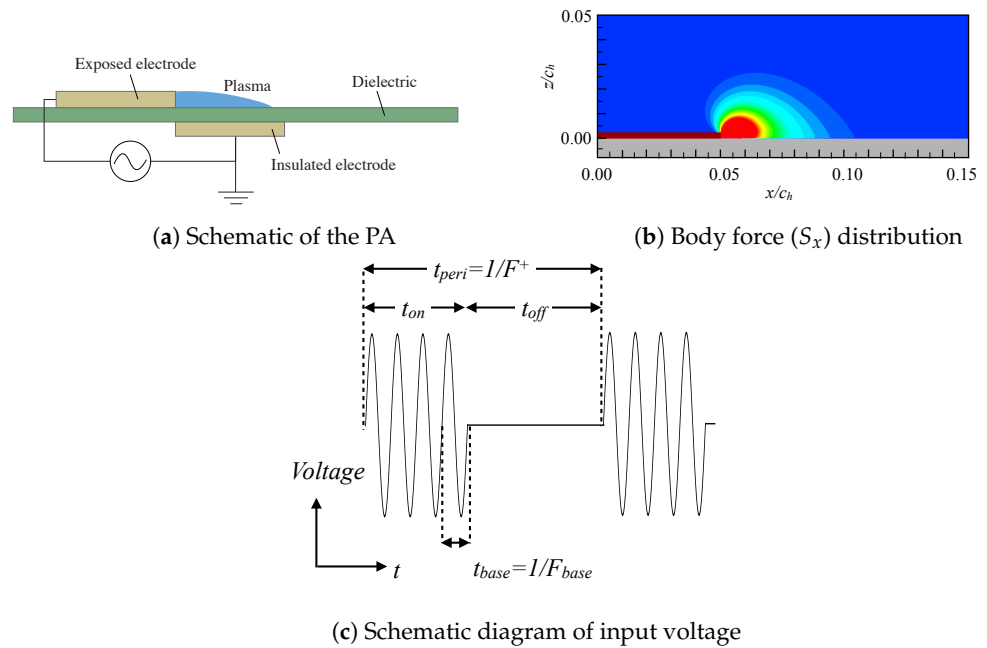


Figure 3. Computational model of the PA.

The strength of the input momentum is defined by the momentum coefficient C_μ as follows:

$$C_\mu = BR \frac{D_{c;effe} \iint_{\Omega} S_{x;suzen} dx dz}{\rho_\infty u_\infty^2 c_h / 2}, \tag{10}$$

where $D_{c;effe}$ is defined as a time average of the unsteady body force as

$$D_{c;effe} S_{suzen} = \frac{1}{t_{on}} \int_0^{t_{on}} D_c S_{suzen} \sin^2(2\pi F_{base}^+ t) dt = \frac{1}{2} D_c S_{suzen}. \tag{11}$$

The momentum coefficient C_μ is generally used in those microdevices for active flow control. Meanwhile, the definition of C_μ is significantly different between the SJ and the PA as described in this study. It is not yet clear if matching C_μ with the present definitions would lead to a fair comparison rigorously; however, as a starting point, we would like to adopt the momentum coefficient as a uniform criteria on the intensity of flow control.

Finally, from a more practical standpoint, atmospheric conditions external to the PA and SJ would impact their controllability. Lilley et al. [34] conducted experimental research in which water droplets were directly sprayed on the PA electrodes to assess the performance of the DBD-PA under rain. They discovered that the thrust is generally decreased due to droplet adhesion at the beginning stage, which is gradually restored depending on the applied voltage and operating frequency. Tanaka et al. [35] installed DBD-PAs on a 300 kW wind turbine and conducted the flow-control experiment, which included the installation of a protection system on the power supply to prevent unanticipated discharge in rainy conditions. Based on our internal communication, the actuation was stopped during the rain and restarted after the rain stopped; the plasma was successfully generated after approximately one rotation of the blade due to the water droplets adhering to the blade surface being blown away by the external flow. A number of researchers have also investigated the performance of the PA under varying humidity conditions [36,37]. The SJ would show fewer difficulties with actuation than the PA due to the absence of exposed electrodes, as reported by Weigel et al. [38], for instance. In terms of detailed flow physics, however, such as the control of the LSB, external atmospheric conditions have not yet been rigorously examined; therefore, the application of the PA and SJ in practical conditions should be attempted with caution.

2.4. Case Description

The computational cases for separation control using the SJ and the PA are summarized in Table 1.

Table 1. Computational cases. Both of the PA and the SJ are installed on the leading edge.

Case Name	Input Momentum (C_μ)	F^+
strong input (SJ)	2.00×10^{-3}	1.0, 6.0, 10, 15, 20, 30
strong input (PA)	2.00×10^{-3}	1.0, 6.0, 10, 15, 20, 30
weak input (SJ)	2.00×10^{-5}	1.0, 6.0, 10, 15, 20, 30
weak input (PA)	5.15×10^{-5}	1.0, 6.0, 10, 15, 20, 30

In order to compare the capabilities of the SJ and the PA, both of the strong and weak input momentum cases were considered. The momentum coefficient, C_μ , was similar to or smaller than that in the previous studies, e.g., $C_\mu = 3.5 \times 10^{-3}$ in [7]. Note that the weak C_μ values are different between the SJ and the PA: $C_\mu = 2.00 \times 10^{-5}$ and 5.15×10^{-5} are set for the SJ and the PA, respectively. This is because the PA with $C_\mu = 2.00 \times 10^{-5}$ was not able to control the separation, while the SJ with the same C_μ successfully suppressed the separation. Since the present study aims to clarify a common mechanism for suppressing the separated flow, it was preferred that the similar controlled flows were compared between the SJ and the PA. The PA with $C_\mu = 5.15 \times 10^{-5}$ was able to suppress the separation, and the input disturbance of $C_\mu = 5.15 \times 10^{-5}$ is close to the minimum input controllable case using the PA. The definitions of C_μ are different between the SJ and the PA, wherein the maximum velocity at the orifice exit and the spatial integral of the time-averaged body force are adopted for the SJ and the PA, respectively. Such a difference in the definition of C_μ can lead to the difference in the minimum controllable C_μ . The details of induced flows will be discussed in Section 4.1, wherein the cases with different C_μ , e.g., $C_\mu = 2.00 \times 10^{-5}$ and 2.00×10^{-6} , were additionally considered for the ease of comparison and data availability from the previous studies [32].

3. Methodology

3.1. Flow Solver

In the present study, LANS3D [39] was employed for the series of computations. LANS3D is a high-order compressible flow solver for structured grids, which was developed at the ISAS/JAXA and applied to a considerable number of engineering problems [13,40], and the capability of the code has been sufficiently verified through the literature above. The governing equations were the three-dimensional compressible Navier–Stokes equations in body-fitted coordinates. The spatial derivatives of the convective and viscous terms were evaluated by a sixth-order compact finite-difference scheme [41]. The metrics and Jacobian for the coordinate transformation were evaluated by the symmetric conservative forms [42,43]. The metrics form can avoid a freestream preservation error on moving and deforming grids even with the high-order compact scheme, which was utilized for simulating the cavity deformation of the SJ. The body force and energy terms for the simulations of the PA were added to the governing equation as described in Equation (5). A tenth-order filtering [44] was used with a filtering coefficient of 0.495, and a numerical oscillation was suppressed. Time integration is conducted by a backward second-order difference formula converged by the five subiterations [45] of the lower-upper symmetric alternating direction implicit and symmetric Gauss–Seidel (ADI-SGS), and the second-order of accuracy in time is ensured. An implicit LES approach (ILES [45,46]) was adopted for turbulent modeling. The ILES approach, unlike the standard LES approach, employs no additional stress and heat flux as the subgrid-scale (SGS) models. Instead, a high-order low-pass filter selectively damps only poorly resolved high-frequency waves.

3.2. Computational Grids and Boundary Conditions

The computational grid was constructed based on the zonal grid approach [47]: background grid around an airfoil (Zone 1), intermediate region (Zone 2), the cavity of the SJ (Zone 4), and the orifice of the SJ (Zone 3) were generated separately, as shown in Figure 4. Zones 1 and 2 were adopted for the PA simulations, where the body force was not directly mapped to the background grid (Zone 1) but to the intermediate grid (Zone 2) for simplicity as well as enhancement in the resolution. The C-type grid was adopted around the airfoil, and the outer boundary was located at $25c_h$ away from the leading edge. The size of the computational domain in the spanwise direction (y direction) was $0.2c_h$. The boundary-fitted coordinate system (ξ, η, ζ) was employed as shown in Figure 4; the minimum grid size in the wall-normal direction (ζ direction) was 0.12% of the chord length c_h (or $0.03/\sqrt{Re}$). The grid of the cavity (Zone 4) was deformed periodically in time, where the grid points were determined in the algebraic manner given by [8,48]. On the boundaries where the zonal grids were connected with each other, approximately 20 grid points were overlapped and the flow variables were exchanged with small errors [47]. The total number of grid points was approximately 30 million (Table 2). At the outflow boundary, all variables were extrapolated from the points next to the outflow boundary. A periodic boundary condition was applied to the spanwise direction. An adiabatic no-slip condition was adopted on the surface of the airfoil and the walls in the SJ. The nondimensionalized computational time step was $\Delta t^* u_\infty / c_h = 4.0 \times 10^{-5}$ and the corresponding maximum Courant number became approximately 1.6.

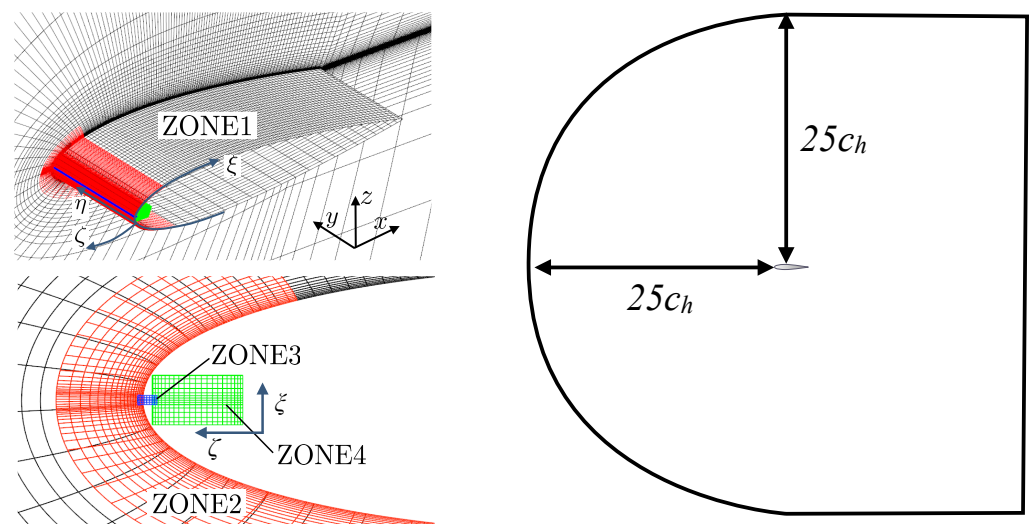


Figure 4. Computational grids (every 5 points are visualized) and coordinates.

Table 2. Number of grid points. (N_ξ, N_η, N_ζ) represents the number of grid points in each direction.

Zone Name	Description	N_ξ	N_η	N_ζ	Number of Grid Points
Zone 1	airfoil grid	795	134	179	19,068,870
Zone 2	intermediate grid	253	134	91	3,085,082
Zone 3	orifice grid	45	134	75	452,250
Zone 4	cavity grid	157	134	214	4,502,132

3.3. Validation and Verification

First, the validation and verification for the PA actuation are described. The flow solver, the PA model, and the computational grids used in this study are the same as those in Sato et al. [13], although C_μ is not the same. For example, in Figure 6a of Sato et al. [13], the mean pressure coefficient along the airfoil surface was compared between the simulation and experiment for non-controlled and controlled cases with $C_\mu = 2.06 \times 10^{-4}$ and

$F^+ = 1.0$ and 6.0 . The results are reasonably agreed well with each other, and thus the simulation in the present manuscript is sufficiently validated.

For the SJ actuation, the same flow solver with the present SJ model was used in Abe et al. [10], wherein an experimental comparison for the non-controlled case and grid/span length/time-step-size convergence studies for the controlled case were carried out. For example, Figure 20 of Abe et al. [10] shows a good agreement with the experimental result on the pressure coefficient along the airfoil surface; Figures 21 and 22 in Abe et al. [10] show the grid convergence results for the controlled case with $F^+ = 6.0$ and $C_\mu = 2.0 \times 10^{-3}$. Those verifications and validations sufficiently support the present simulation, including the flow solver and computational grid for the SJ cases.

4. Results and Discussion

4.1. Differences of Induced Flows from the SJ and the PA

In this study, C_μ is utilized as a criterion for characterizing the strength of the input momentum from each device, as it has been in previous studies [4,6,9,13,19,49]. However, the definitions of C_μ are different for the SJ and the PA because the operation mechanism and properties of induced flows are different. For example, the time average of the induced flow of the PA has the velocity in the direction from the exposed to the insulated electrode. Meanwhile, the time average of the induced flow, strictly a net input momentum, is zero in the SJ, as the blowing and suction phases periodically occur. This section discusses differences in the induced flow from the SJ and the PA, wherein the following four items are taken into account:

- A. Wall-tangential velocity;
- B. Three-dimensional flow structures;
- C. Spatial locality;
- D. Temporal fluctuation.

A. Wall-Tangential Velocity

Figure 5b,c represent the phase- and spanwise-averaged velocity at the SJ's orifice exit, with u_{jet} in the wall-normal (normal to the orifice exit) component and w_{jet} in the wall-tangential (along the orifice exit) component. Figure 5a 1 depicts the phase diagram of cavity deformation. The notations u_{jet} and w_{jet} relate to the flows around the airfoil, with the negative value for the u_{jet} corresponding to the blowing operation. The horizontal axis x_{orifice} represents the coordinate along the orifice exit plane (note the red line in the orifice of Figure 5d), which is at half depth on the orifice section. Solid and broken lines represent the blowing phase ($\varphi = \pi/2$) and the suction phase ($\varphi = 3\pi/2$), respectively. The results of four different C_μ including the strong and weak input cases of Table 1 with the fixed actuation frequency of $F^+ = 6$ are compared. w_{jet} (wall-tangential component) is approximately 10% of u_{jet} (wall-normal component), so u_{jet} characterizes the induced flow of the SJ in all input momentum cases. The three cases ($C_\mu = 2.0 \times 10^{-3}$, 2.0×10^{-4} , and 2.0×10^{-5}) suppressed the separation; however the $C_\mu = 2.0 \times 10^{-6}$ condition was unable to manage the separation. At the suction phase, w_{jet} and u_{jet} have asymmetric profiles with respect to the orifice center ($x_{\text{orifice}} = 0$). This occurs because the external flow crosses the orifice exit, where the internal flow is entrained downstream ($x_{\text{orifice}} > 0$). When the SJ is in a quiescent flow, the profiles become symmetric, according to [8], and the wall-tangential flow component approaches zero. Furthermore, Figure 5d demonstrates the vortical structures inside the cavity in the case of $C_\mu = 2.0 \times 10^{-3}$ and $F^+ = 6.0$, where the isosurface corresponds to the second invariant of the velocity gradient tensor colored by the chordwise vorticity. The flow inside the cavity shows a strong three-dimensional structure, which will be described by the turbulent component of the phase-averaged velocity in the next part B.

It is difficult to identify the induced velocity of the PA during the separation control due to the existence of external flows. On the other hand, the body force distribution of the PA in Figure 3b suggested the existence of the wall-tangential component of the induced

flow. Therefore, the momentum in the freestream direction was more directly introduced from the PA than the SJ, which can be regarded as one of the differences in the separation control mechanisms, especially for the strong C_μ cases.

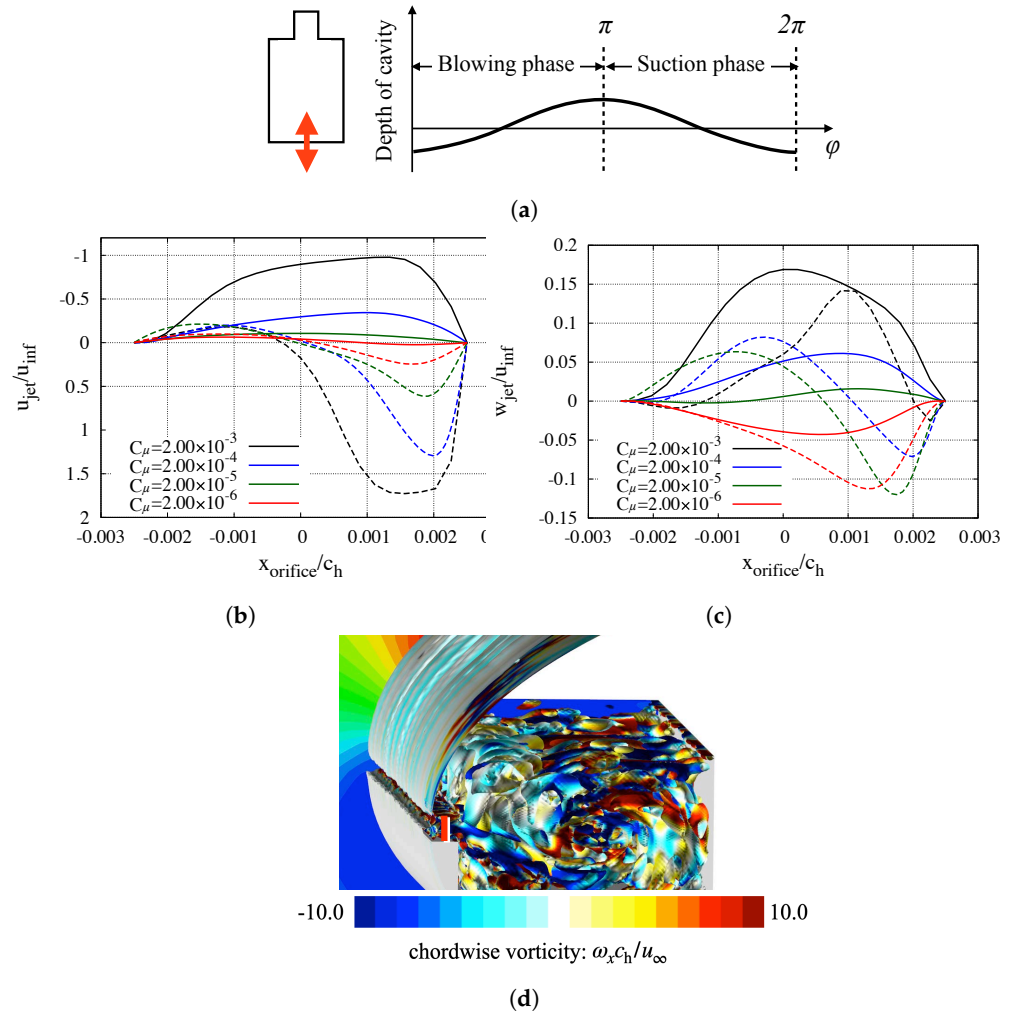


Figure 5. Profile of phase-averaged velocity inside the orifice of SJ with $F^+ = 6.0$: (a) the phase diagram; (b) wall-normal velocity (solid and dashed lines represent the blowing and suction phases, respectively); (c) wall-tangential velocity (solid and dashed lines represent the blowing and suction phases, respectively); and (d) instantaneous vortex structures within the cavity ($C_\mu = 2.0 \times 10^{-3}$, $F^+ = 6.0$). The isosurface of (d) corresponds to the second invariant of the velocity gradient tensor and is colored by the chordwise vorticity normalized by the uniform flow: $\omega_x c_h / u_\infty$.

B. Three-Dimensional Flow Structures

The turbulent component of the spanwise fluctuation inside the orifice is shown in Figure 6. The actuation frequency was set to $F^+ = 6.0$, and the measurement line is identical to that shown in Figure 5. The blowing and suction phases are shown by solid and dashed lines ($\varphi = \pi/2$ and $3\pi/2$, respectively). The greater the C_μ , the larger the turbulent component of the fluctuation within the cavity, indicating three-dimensional structures in the generated flow. Similar effects of C_μ on the three-dimensional induced flow were observed in the prior work for the quiescent flows [8]. The instantaneous vortices within the cavity for three distinct C_μ at each phase from $\varphi/2\pi = 1/10$ to $9/10$ are shown in Figure 7, where the isosurface depicts the second invariant of the velocity gradient tensor colored by the chordwise (x -axis) vorticity. These visualizations show that, in contrast to the weak C_μ simulation, the strong C_μ case forms the three-dimensional structures within the cavity.

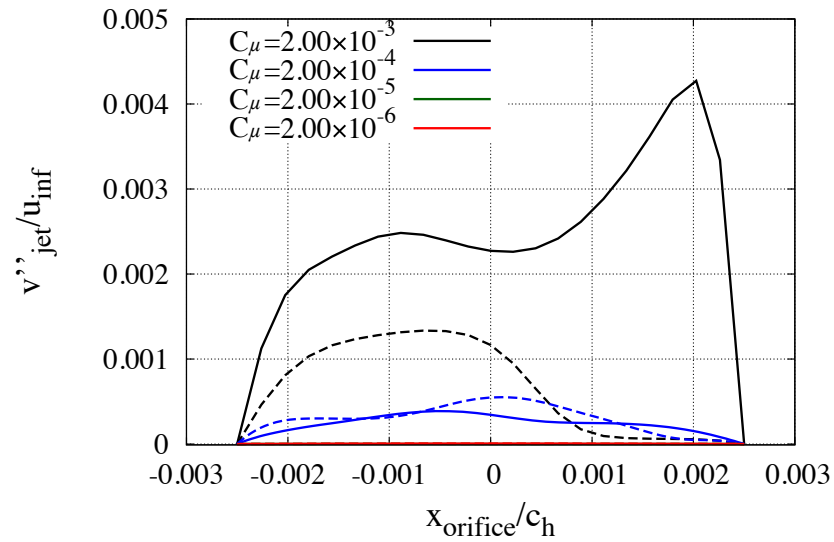


Figure 6. v''_{jet} is the turbulent component of the phase-averaged velocity profile within the orifice of SJ with $F^+ = 6.0$. The blowing ($\varphi = \pi/2$) and suction ($\varphi = 3\pi/2$) phases are shown by solid and broken lines, respectively.

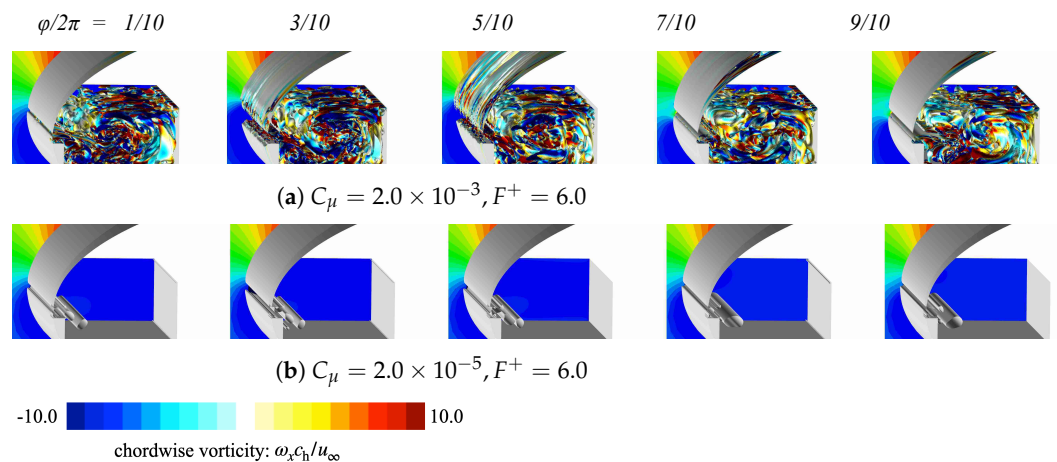


Figure 7. (a) Structure of instantaneous vortices in the SJ cavity for various C_μ and $F^+ = 6.0$. The figures are taken from Figure 9 in [10]. The isosurface of (b) corresponds to the second invariant of the velocity gradient tensor and is colored by the chordwise vorticity normalized by the uniform flow: $\omega_x c_h / u_\infty$.

The body force model for the PA, on the other hand, used spanwise-uniform profiles, preventing the PA from generating three-dimensional structures. As a result, one of the discrepancies between the SJ and the PA in the current computational models occurs in the spanwise fluctuation (three-dimensional structure) when C_μ is high, which could influence the promotion of a turbulent transition in the separated shear layer around the leading edge. Since the weak input momentum situations ($C_\mu = O(10^{-5})$) do not exhibit large spanwise variation even in the SJ, there are little variances between the induced flow from the SJ and the PA in these circumstances. On the other hand, the extraction of the induced flow by the PA under flow control was not realizable due to the existence of the external flow. To partly support the present discussion, the instantaneous vortex structures which will be discussed in detail later in Figure 16 can be referred herein. The strong input momentum case showed three-dimensional fluctuation only in the SJ cases. It should also be noted that recent experimental and numerical simulations of the PA revealed the presence of

a three-dimensional body force [50,51]. The effects on the three-dimensional unsteady flow motion, such as a turbulent transition, have not been adequately addressed, despite evidence that such spanwise fluctuation of the body force has little effect on an induced flow in terms of the time and spanwise-averaged characteristics [50].

C. Spatial Locality

The power spectral density (PSD) of the wall-normal fluctuation at the leading edge in the separation control utilizing a weak input with $F^+ = 6.0$ is shown in Figure 8. The PSDs are taken at each x/c_h point when the turbulent kinetic energy (TKE) reaches its highest. The peak of the SJ and the PA is at $F^+ = 6.0$, and its harmonics are enhanced downstream. The PSD of $Fp = 6.0$ at the leading edge, on the other hand, is approximately 10 times greater in the SJ than in the PA, despite the fact that C_μ was adjusted to be almost identical ($C_\mu = 2.00 \times 10^{-5}$ for the SJ; $C_\mu = 5.15 \times 10^{-5}$ for the PA). This suggests that the wall-normal fluctuation at the referred location is different, despite the fact that the input momentum is in the same order.

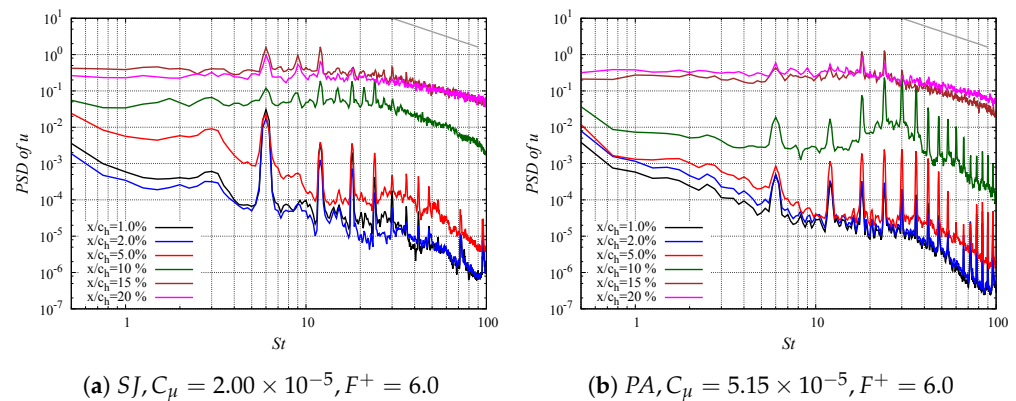


Figure 8. PSD of wall-tangential fluctuation in the separated shear layer during control. The grey straight line illustrates Kolmogorov's 5/3 law. The figure (a) is taken from Figure 11 in [10].

The spatial profiles of time- and spanwise-averaged induced flow of the SJ and PJ are presented in Figure 9. In the controlled situations, the induced flow of the SJ was calculated from the flow field within the orifice, using the root-mean-square for the wall-normal component (w_{jet}) at half the depth of the orifice. The vertical axis of Figure 9 corresponds to the horizontal axis (the coordinate along the orifice exit x_{jet}) in Figure 5a,b for awareness. Because the induced velocity of the PA cannot be measured during separation control, the induced flow of the PA was estimated in the quiescent flow and obtained from [32]. The coordinate in the wall-normal direction corresponds to the vertical axis of Figure 9. The velocity profile in Figure 9 (solid lines represent the SJ; dotted lines show the PA) shows that the induced flow is more confined in the SJ than in the PA. This tendency for the localization would be predicted in the separation-controlled flow employing the PA, as illustrated in the induced-flow schematic of Figure 10. The boundary layer covers the leading edge where the SJ and the PA are implemented under the current flow/actuator circumstances. Because the thickness of the boundary layer is so thin at the leading edge, the SJ can introduce the fluctuation into the boundary layer more efficiently than the PA. Since the SJ introduces a larger amount of fluctuation to the boundary layer than the PA, the PSD in the separated shear layer would be impacted, as seen in Figure 8.

Finally, the width of the orifice can alter the spatial profiles of the flow induced by the SJ. In addition, the distance between the separated shear layer and the orifice exit is highly dependent upon the flow condition (e.g., angle of attack), airfoil, and location of the SJ. As a result, the spatial localization of the SJ-induced flow is not necessarily superior to that of the PA, which should be carefully considered under the various flow/actuator settings.

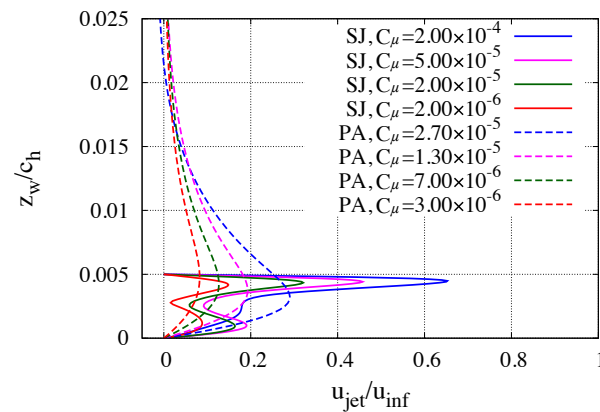


Figure 9. Time-averaged velocity fluctuation.

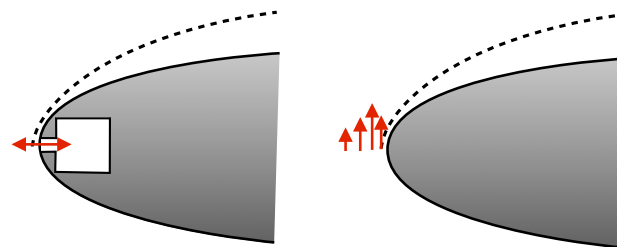


Figure 10. The flows induced by the SJ (**left**) and by the PA (**right**) are shown schematically. The grey area depicts a zoomed-in view of an airfoil's leading edge; red arrows indicate induced fluctuation; and black dotted lines depict separation streamlines.

D. Temporal Fluctuation

As can be seen from the PSD of the wall-normal fluctuation in Figure 8, the power distribution of high-frequency modes at $St \simeq 100$ is greater in the PA than in the SJ around the leading edge, where the fluctuation directly impacts its profile. As a result, the temporal variation of the induced flow causes the difference between the SJ and the PA in such a high-frequency domain. The higher ($St \geq 100$) frequencies in the induced flow are included in the PA owing to the base frequency of the AC input voltage. The differences in the time history of input fluctuations are clearly seen in Figures 2 and 3c. Previous research for the PA [13,32], which used the burst mode (duty cycle), found a comparable trend in the large amplitude of higher-frequency fluctuation ($St \geq 100$).

The simulation of the SJ with burst actuation with the base frequency of $F^+ = 100$ was additionally conducted in the quiescent flow, and the effect of the base frequency was clarified. Blue and red lines in Figure 11 show the PSDs of the burst and normal actuation with the base frequency, respectively. For the wall-normal component of the flow velocity, the PSD was measured at the orifice exit. The data clearly reveal that in the burst actuation with base frequency, the PSD of higher frequencies ($St \simeq 100$) was much greater than in the normal actuation case. This indicates that the burst actuation is capable of introducing the higher frequency fluctuations of the base frequency into the induced flow. In separation-controlled conditions, such a high-frequency mode directly affects the nonlinear evolution of turbulent fluctuation, which occurs at a higher frequency than shear layer instability. The modulation of the base frequency, on the other hand, has no effect on the capacity of the separation control utilizing the burst actuation of the PA [13]; however, the differences from the normal actuation without such higher-frequency fluctuation were not fully explained.

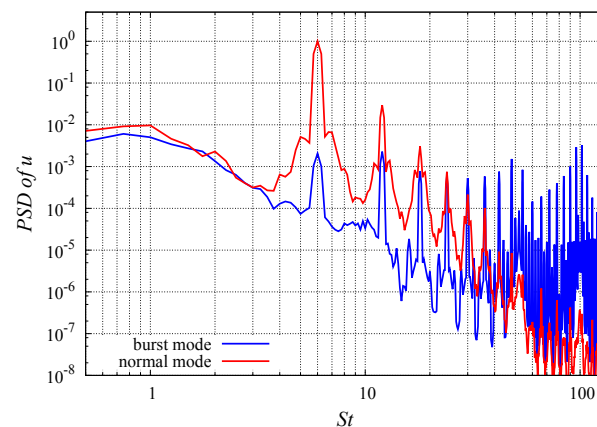


Figure 11. PSD of wall-normal velocity fluctuation induced by the SJ in the quiescent air (red is the normal mode; blue is the burst mode).

4.2. Capabilities of Separation Control

In this section, the separation-control capabilities were evaluated with regard to time-averaged aerodynamic coefficients. The time-averaged aerodynamic coefficients are shown in Figure 12, where the horizontal axis represents the actuation frequency F^+ and the vertical axis represents each time-averaged coefficient employing the SJ and the PA. The strong, weak, and non-controlled cases are shown by the red, blue, and black lines, respectively. The results of the SJ and the PA are shown by solid and dashed lines, respectively. Throughout this work, the control capabilities were assessed using the time-averaged lift-to-drag ratio (C_L/C_D). For either strong or weak input momentum, C_L/C_D was largely recovered in both SJ and PA at approximately $6 \leq F^+ \leq 20$. There is a localized range of frequencies where the separation is effectively suppressed, which is not significantly different between two devices. Therefore, the controlled flow fields of $F^+ = 1.0$ and 6.0 are mainly focused, and the mechanism of the localization of the optimal actuation frequencies is discussed hereafter.

Here, C_L/C_D of the PA was lower than that of the SJ for $6.0 \leq F^+ \leq 15$ in the weak C_μ cases. Moreover, only the SJ was able to suppress the separation in the case of $F^+ = 20$. In circumstances when the C_μ was low, the SJ exhibited greater control capabilities across a broader range of F^+ , despite the fact that the PA's C_μ was nearly double that of the SJ. A difference of this magnitude would be the result of the spatial locality in the induced flow (C in Section 4.1). In the current model parameters, the maximum amplitude of the velocity fluctuation introduced by the devices into the separated shear layer is greater by the SJ than the PA. As a result, a turbulent transition starts in the upstream region, and the SJ maintains the size of the separation bubble smaller (see the red lines in Figure 14).

On the other hand, no significant difference was observed in the cases with the strong C_μ ($C_\mu = 2.00 \times 10^{-3}$). C_L/C_D was recovered by any F^+ , and the C_L was slightly better in the PA than in the SJ. The wall-tangential momentum which is directly introduced from the device can effectively modify the separated flow in these strong C_μ cases. As was discussed in A of Section 4.1, the PA can more directly introduce the momentum in the wall-tangential direction than the SJ, which leads to the difference in the C_L with strong C_μ . It is also noteworthy that later in Figure 14, the separation bubble using the SJ is smaller than using the PA, which indicates that the turbulent transition in the SJ occurs at a more upstream position than the PA. Therefore, enhancing the shear layer instability by the three-dimensional and localized flows induced by the SJ (see B and C of Section 4.1) can be less effective in the strong C_μ cases than injecting the direct momentum from the PA.

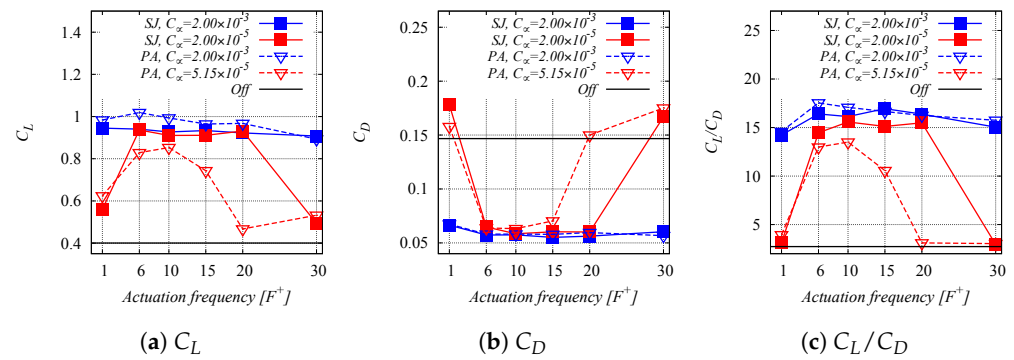


Figure 12. Time-averaged C_L , C_D , and C_L/C_D are summarized. Solid and dashed lines represent the results of the SJ and the PA, respectively. The blue and red lines are strong and weak C_μ cases, respectively.

4.3. Flow Fields of Controlled Cases

The time- and spanwise-averaged chordwise velocity, u/u_∞ , in the cases of $F^+ = 1.0$ and 6.0 are shown in Figure 13. As shown in Figure 13a–d, attached flows were obtained by both SJ and PA in cases with strong C_μ . A separation bubble was formed on the leading edge, with the size of the bubble being smaller in $F^+ = 6.0$ than 1.0 . A similar trend was seen in the reversed flow area depicted in Figure 14. Figure 14 shows that the size of the separation bubble decreases when SJ is used instead of PA for each actuation condition. This difference can be explained by the position of a turbulent transition in the separated shear layer. Figure 15 shows the time-averaged pressure coefficient along the airfoil surface. Figure 15a,b show the controlled cases with $F^+ = 1.0$ and 6.0 , respectively, as well as the non-controlled case. In the controllable cases, pressure plateau regions are observed near the leading edge at approximately $x/c_h \simeq 0.1$. Note that the controlled cases with $C_\mu = 2.0 \times 10^{-3}$ and $F^+ = 6.0$ for both SJ and PA in Figure 15b do not clearly show the plateau region; those pressure distributions correspond to the separation bubbles represented in Figure 14.

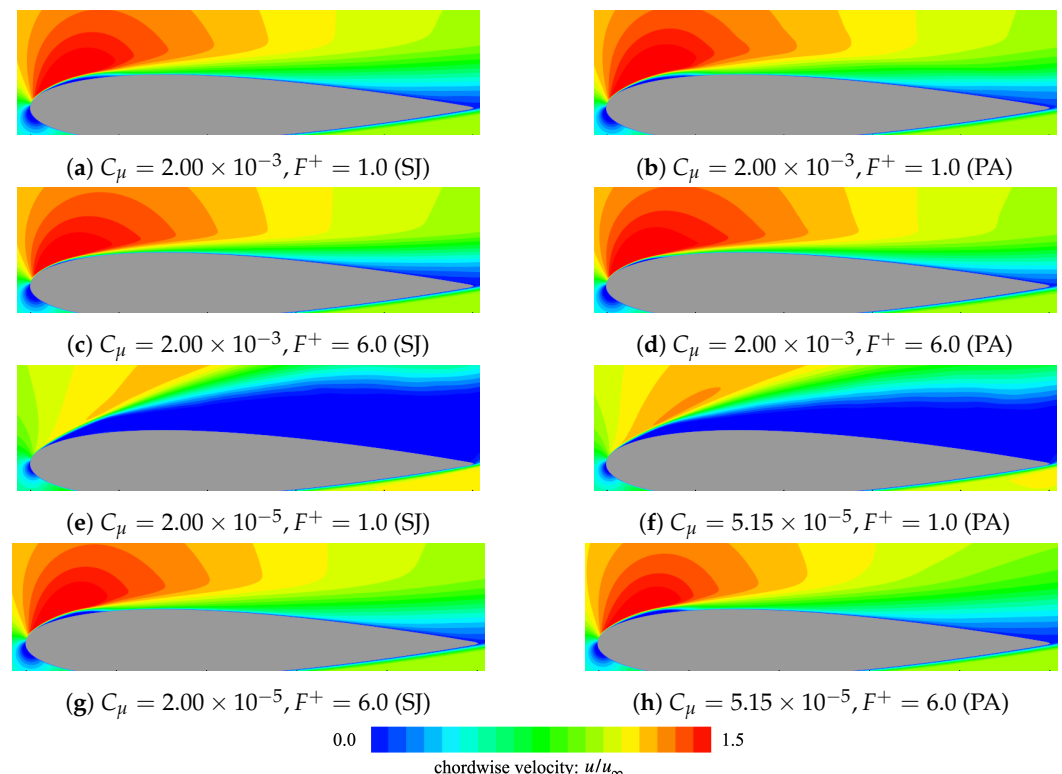


Figure 13. Time- and spanwise-averaged fields of u/u_∞ colored between 0.0 and 1.5.

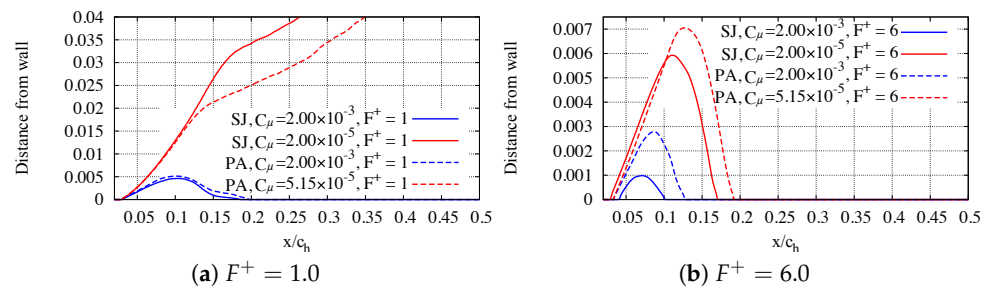


Figure 14. Reversed flow region near the leading edge: Solid and dashed lines show the reversed flow region around the leading edge using the SJ and the PA, respectively. Red and blue lines indicate the weak and strong input momentum, respectively.

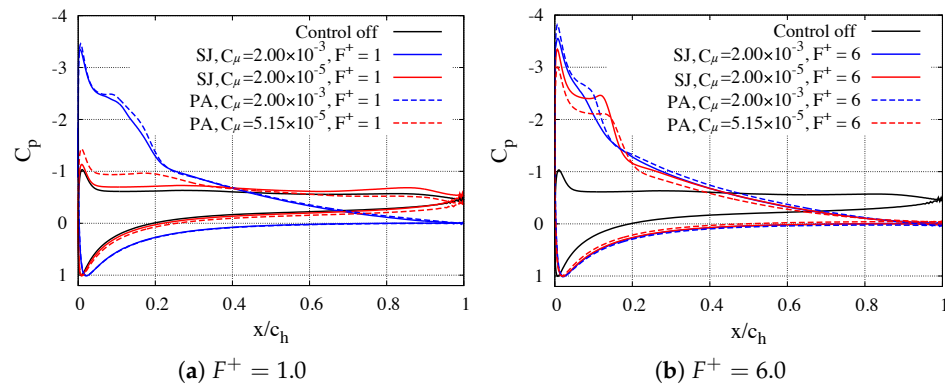


Figure 15. Time-averaged pressure coefficient along the airfoil surface.

Figure 16 shows the instantaneous flow fields. The isosurface is a second invariant of the velocity gradient tensor colored by the chordwise (x -directional) vorticity. In each case, two-dimensional (spanwise-uniform) vortex structures are emitted from the separated shear layer, then they are convected in the downstream direction with amplifying three-dimensional fluctuations. The separated shear layer is mostly laminar, then it reattaches to the airfoil surface and a turbulent boundary layer is formulated, when the separation is suppressed, i.e., except for the cases with $F^+ = 1.0$ of the weak C_μ for the SJ and the PA. Thus, the separation bubble can be thought of as a laminar separation bubble in those cases. Note that in the case with the strong C_μ , the SJ introduces three-dimensional fluctuation near the leading edge, while the PA only introduces the two-dimensional fluctuation (see B in Section 4.1).

4.4. Phase Decomposition of Turbulent Statistics

The phase decomposition of an instantaneous quantity $f(t)$ is introduced as

$$f(t) = \underbrace{\bar{f}}_{\text{overall average}} + \underbrace{\tilde{f}_\varphi}_{\text{periodic fluc.}} + \underbrace{f''(t)}_{\text{turbulent fluc.}} = \underbrace{\langle f \rangle_\varphi}_{\text{phase average}} + \underbrace{f''(t)}_{\text{turbulent fluc.}}, \quad (12)$$

where the total and phase-averaging operators are defined as $\bar{\bullet}$ and $\langle \bullet \rangle_\varphi$, respectively. Based on the decomposition of Equation (12), a time-averaged correlation of fluctuations, $f'(t)$ and $g'(t)$, can be

$$\overline{f'g'} = \overline{\tilde{f}_\varphi \tilde{g}_\varphi} + \overline{f''g''}. \quad (13)$$

The periodic and turbulent components of the Reynolds shear stress are shown in Figure 17: $\overline{u'w'} = \overline{\tilde{u}\tilde{w}} + \overline{u''w''}$. A spanwise averaging was also performed; however, the symbol for this operation was deleted for brevity's sake. The Reynolds stress $\overline{u'w'}$ represents the correlation between the velocity fluctuation in the x and z directions. This corresponds to the exchange of momentum in the chordwise direction, which shows

how the momentum can be entrained from the external freestream into the near-wall surface. The overall component of $\overline{u'w'}$ is shown in the left column, while the phase and turbulent components, $\overline{u\overline{w}}$ and $\overline{u''w''}$, are shown in the center and right columns, respectively. All the cases demonstrate that the turbulent component $\overline{u''w''}$ is dominant, and hence turbulent structures mostly contribute to momentum exchange in the chordwise direction. In terms of the periodic component, however, there is a small variation between the SJ and the PA. The strong input case ($C_\mu = 2.0 \times 10^{-3}$) with $F^+ = 1.0$ and 6.0 using the PA (Figure 17b,d) has a stronger periodic component at $x/c_h \simeq 0.5$ than the case using the SJ (Figure 17a,c). The lack of three-dimensional (spanwise-nonuniform) variations in the induced flow of the PA (B in Section 4.1) causes this difference. In these strong C_μ situations, two-dimensional vortex structures strongly remain further downstream when utilizing the PA rather than the SJ, as stated in Section 4.5. As a consequence, the exchange of chordwise momentum is mostly produced via turbulent vortex structures independent of devices in the current flow and actuator settings; however a little difference in the intensity of the periodic component arises when the input momentum becomes strong.

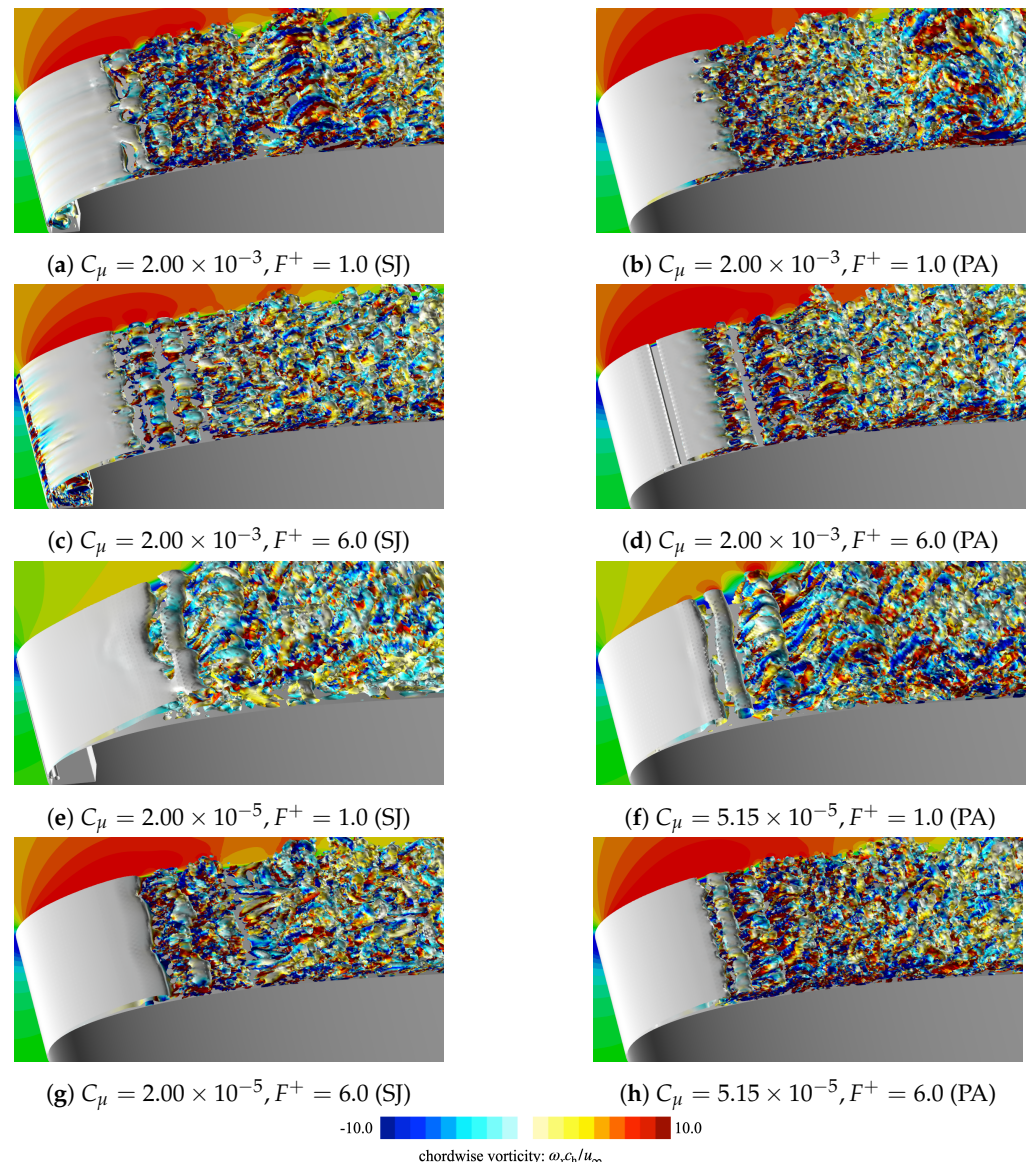


Figure 16. Instantaneous vortex structures around the leading edge. Isosurfaces show the second invariant of the velocity gradient tensor (colored by chordwise velocity u/u_∞ for 0.0 to 1.5). The figures (a,c,g) are taken from Figure 9 in [10].

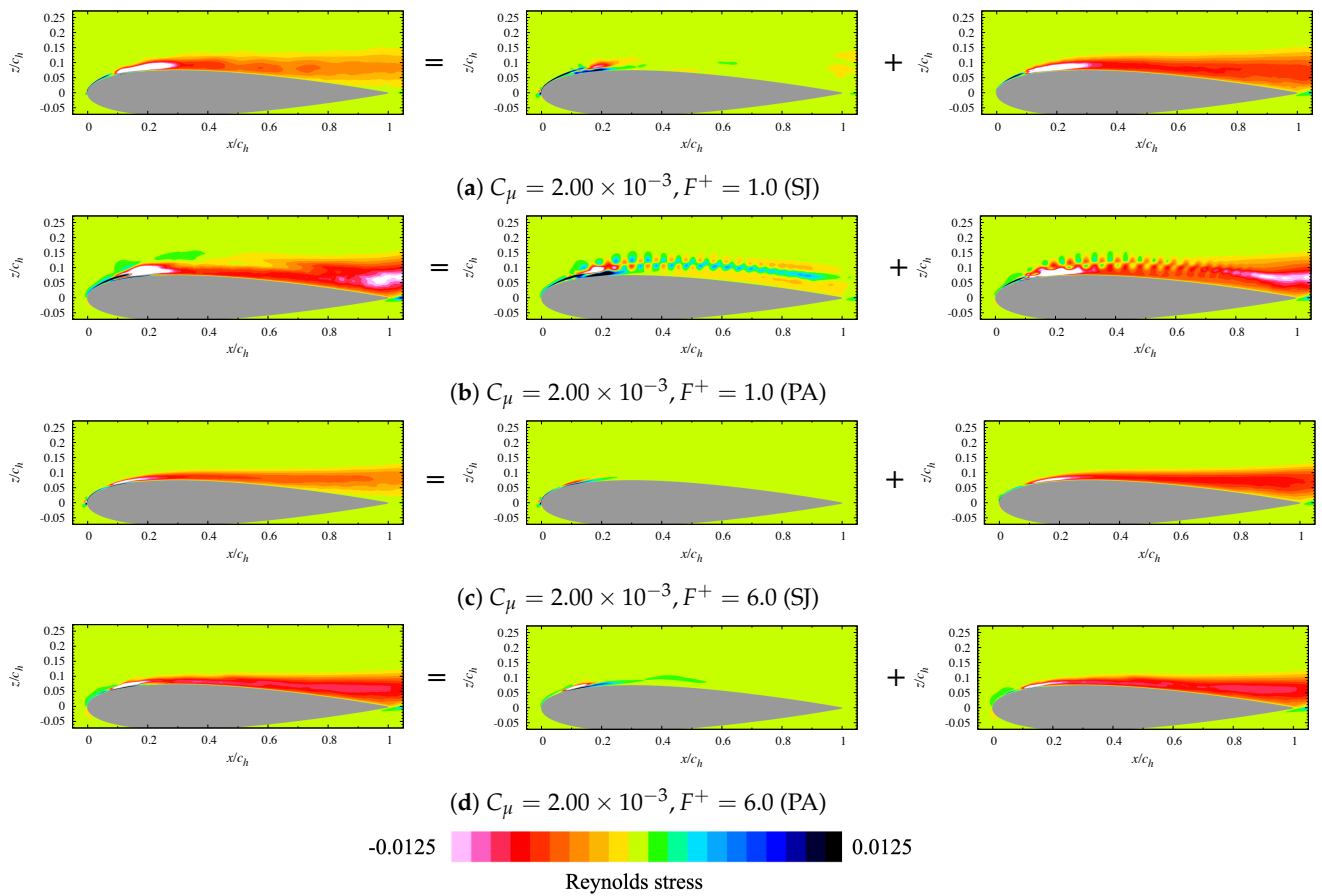


Figure 17. Phase decomposition of the Reynolds shear stress $-\overline{u'w'}/u_\infty^2$. The Reynolds shear stress is decomposed into periodic ($\langle \tilde{u}\tilde{w} \rangle_\varphi$) and turbulent ($\langle u''w'' \rangle_\varphi$) components. The figures (a,c) are taken from Figure 12 in [10].

4.5. Coherent Vortex Structures and Chordwise Momentum Exchange in Phase-Averaged Flow Fields

Based on the decomposition of Equation (12), a phase-averaged correlation of fluctuations, $f'(t)$ and $g'(t)$, can be written as

$$\langle f'g' \rangle_\varphi = \langle \tilde{f}_\varphi \tilde{g}_\varphi \rangle_\varphi + \langle f''g'' \rangle_\varphi, \tag{14}$$

which is applied to the Reynolds shear stress as follows: $\langle u'w' \rangle_\varphi = \langle \tilde{u}\tilde{w} \rangle_\varphi + \langle u''w'' \rangle_\varphi$. The spanwise average was also conducted in addition to the phase averaging procedure. Figures 18 and 19 show $\langle \tilde{u}\tilde{w} \rangle_\varphi$ and $\langle u''w'' \rangle_\varphi$ in the phases from $\varphi/2\pi = 1/10$ to $9/10$. The black contour lines show the second invariant of the velocity gradient tensor in each phase.

The black contour lines in Figures 18 and 19 identified the coherent vortex structures with its axis along the spanwise direction. The number of those vortex structures depends on the actuation frequency F^+ . The coherent vortices are generated in the downstream of the separation bubble near the leading edge. They formed a large single vortex in the case of $F^+ = 1.0$ in Figure 18 and six vortices in the case of $F^+ = 6.0$ in Figure 19. Therefore, both SJ and PA generate the coherent vortex structures in the separation-controlled (attached) flows, which is concealed in the turbulent boundary layer but can be successfully identified by the phase-averaging procedure. The Reynolds shear stress distribution illustrates that the turbulent component $\langle u''w'' \rangle_\varphi$ is dominant over most of the airfoil surface for both SJ and PA. The turbulent component is also locally amplified around the coherent vortices, which is entrained as the coherent vortices convecting in the downstream direction. On the other hand, the periodic component $\langle \tilde{u}\tilde{w} \rangle_\varphi$ in the PA cases appears more strongly than

that in the SJ cases (e.g., Figure 18a,c). This is caused by the spanwise-uniform fluctuation introduced by the PA (B in Section 4.1), wherein the PA does not induce three-dimensional fluctuation and thus the spanwise vorticity remains strongly. The strength of such a coherent vortex can affect the entrainment of the turbulent component of the Reynolds shear stress. Indeed, the turbulent components around the coherent vortices in Figures 18d and 19d are stronger than in Figures 18b and 19b, respectively. Such a difference leads to the more effective exchange of the chordwise momentum using the PA, and thus the aerodynamic performances are better in the PA than in the SJ, as in Figure 12. Another remark on the difference between the SJ and the PA in $F^+ = 1.0$ with $C_\mu = 2.0 \times 10^{-3}$ is that in the PA case, the turbulent component of $\langle u''w'' \rangle_\varphi$ is locally amplified in the vicinity of the trailing edge. Such an amplification is not observed in the SJ case for $\langle u''w'' \rangle_\varphi$. This is again explained by the strength of the spanwise coherent vortex along the suction surface. In the PA, the two-dimensional vortex structure remains stronger even in the aft portion of the airfoil surface, which collapses into a three-dimensional structure near the trailing edge. The similar transition first occurs on the laminar separation bubble near the leading edge, which can be observed both in the SJ and the PA. The PA induces the stronger two-dimensional structure than the SJ, and thus the turbulent component is again amplified near the trailing edge, which is not observed in the SJ case.

In summary, the phase decomposition of the Reynolds shear stress in the separation-controlled flows revealed that the turbulent component mainly contributes to the effective exchange of the chordwise momentum in both SJ and PA cases. On the other hand, in the strong C_μ cases, the coherent vortex structures and periodic component of the Reynolds shear stress are stronger in the PA than in the SJ due to spanwise-uniform fluctuation induced by the PA. Since such coherent vortex structures strongly remain in the downstream direction, the flow is better suppressed by PA than SJ in the strong C_μ cases.

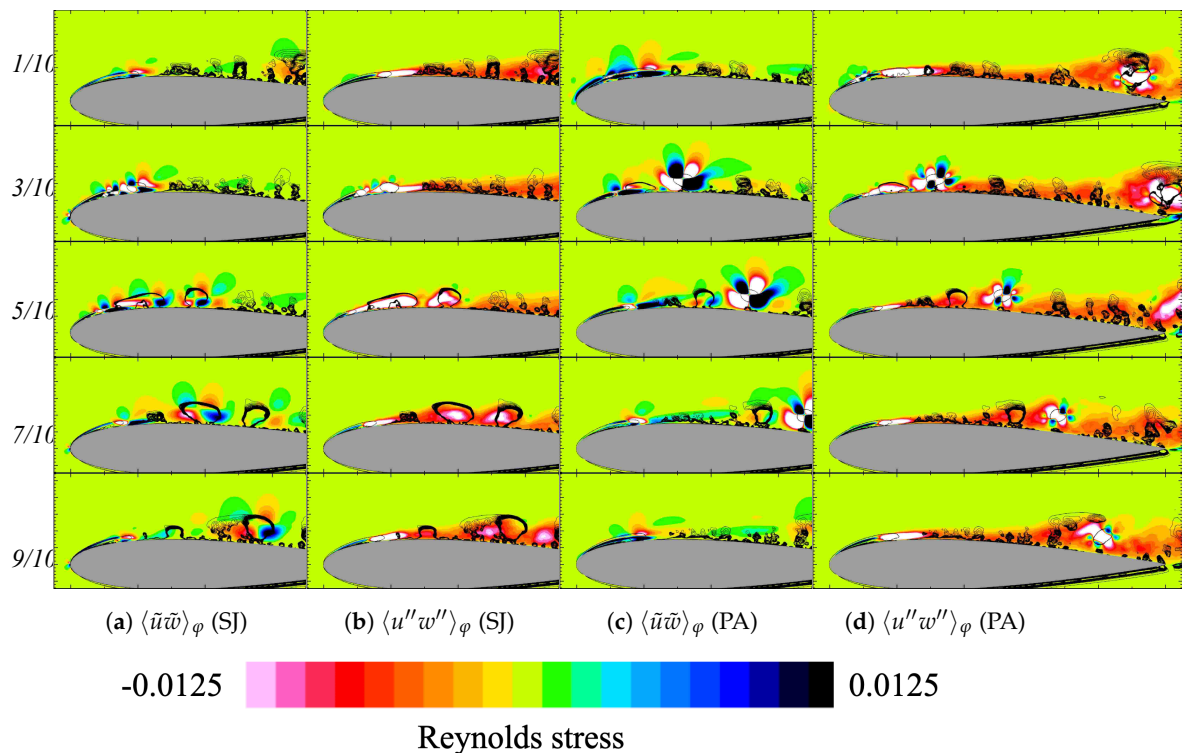


Figure 18. Phase decomposition of the Reynolds shear stress in the case of $C_\mu = 2.0 \times 10^{-3}$, $F^+ = 1.0$. Contour color shows periodic $\langle \tilde{u}\tilde{w} \rangle_\varphi$ and turbulent $\langle u''w'' \rangle_\varphi$ components. Black contours show the second invariant of the velocity gradient tensor in the phase- and spanwise-averaged flow field. The figures (a,b) are taken from Figure 13 in [10].

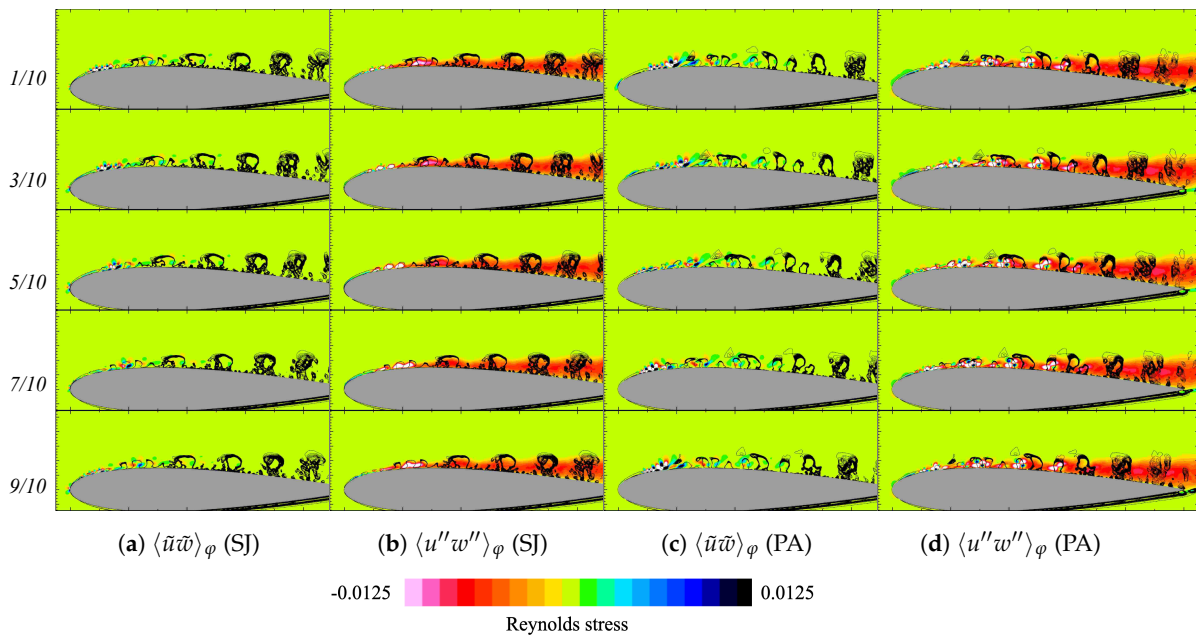


Figure 19. Phase decomposition of the Reynolds stress in the case of $C_\mu = 2.0 \times 10^{-3}$, $F^+ = 6.0$. Contour color shows periodic $\langle \tilde{u}\tilde{w} \rangle_\varphi$ and turbulent $\langle u''w'' \rangle_\varphi$ components. Black contours show the second invariant of velocity gradient tensor in the phase- and spanwise-averaged flow field. The figures (a,b) are taken from Figure 13 in [10].

5. Conclusions

This study numerically investigated the mechanisms of separation control with the SJ and the PA around an NACA0015 airfoil at the chord Reynolds number of 63,000. Both SJ and PA were installed on the leading edge with the same order of input momentum C_μ ($C_\mu = O(10^{-3})$ and $O(10^{-5})$) and the same actuation frequencies between $F^+ = 1.0$ and 30.

First, the induced flows from the present numerical model of the SJ and the PA were compared, and the four main differences were clarified as follows:

- A. Wall-tangential velocity;
- B. Three-dimensional flow structures;
- C. Spatial locality;
- D. Temporal fluctuation.

The item A indicates that the momentum in the wall-tangential direction is less induced by the SJ than the PA. The item B explains that the three-dimensional structure can be generated in the induced flow of the SJ, while the present PA only models the two-dimensional (spanwise-uniform) body force. The item C describes that the flow induced by SJ is spatially localized near the airfoil surface while the velocity induced by PA shows a wider wall-normal distribution. The item D shows that the PA introduces higher-frequency fluctuation ($St = O(100)$) due to the existence of the base frequency, which may contribute to the amplification of higher-frequency modes in the downstream of the separated shear layer. The first two items (A and B) would much affect the capabilities of separation control when C_μ is strong; on the other hand, the last two items (C and D) can appear regardless of the strength of C_μ .

Next, the capabilities and mechanism of separation control were investigated. Separation control by both SJ and PA shows better C_L/C_D in $F^+ = 6.0 - 20$ than in other frequencies. Specifically, the PA recovered C_L/C_D better than the SJ in the strong C_μ cases. In those cases, spanwise-coherent vortices remain further downstream using the PA. In the weak C_μ cases, the SJ recovered C_L/C_D better than the PA for $F^+ = 6.0 - 20$. This is due to the drag reduction by promoting the turbulent transition near the leading edge and decreasing the size of the separation bubble.

As such, there are differences in the induced flows and capabilities of separation control by the SJ and the PA. Nevertheless, the overall mechanisms for separation control in the present condition were similarly identified as follows: The turbulent component of the Reynolds shear stress mainly contributes to the exchange of the chordwise (streamwise) momentum; and the turbulent vortices are convected over the airfoil surface by the coherent spanwise vortices with the frequency of F^+ . We believe that those common and different mechanisms for separation control can be applied to more general devices as long as they are operated with a small input momentum such as $C_\mu = O(10^{-3} - 10^{-5})$ and the separated flow is in the low Reynolds number of $Re = O(10^{-4})$ and at a low angle of attack.

Author Contributions: Conceptualization, Y.A., T.N. and K.F.; methodology, Y.A., M.S., H.A. and T.N.; software, Y.A., M.S., H.A. and T.N.; validation, Y.A., M.S., H.A. and T.N.; formal analysis, Y.A., M.S., H.A. and T.N.; investigation, Y.A.; resources, Y.A., M.S., H.A. and T.N.; data curation, Y.A.; writing—original draft preparation, Y.A.; writing—review and editing, Y.A., M.S., H.A., T.N. and K.F.; visualization, Y.A., M.S., H.A. and T.N.; supervision, T.N. and K.F.; project administration, K.F.; funding acquisition, K.F. All authors have read and agreed to the published version of the manuscript.

Funding: The present study was mainly supported by a Grant-in-Aid for JSPS Fellows (Grant Number 258793) and in part by Strategic Programs for Innovative Research (SPIRE) of the High-Performance Computing Initiative (HPCI) (Project IDs: hp120296, hp130001, hp140207, and hp150219). The computations in the present study were performed using the “K” supercomputer at the Advanced Institute of Computational Science, Riken, Japan.

Institutional Review Board Statement: Not applicable.

Informed Consent Statement: Not applicable.

Data Availability Statement: Not applicable.

Conflicts of Interest: The authors declare no conflict of interest.

Appendix A. Results of Higher F^+ Actuation

This appendix summarizes some of the results with higher F^+ , which were not shown in the main context. Figure A1 presents the instantaneous flow fields for $C_\mu = 2.0 \times 10^{-3}$ with $F^+ = 10, 20,$ and 30 . As in the lower frequency cases, two-dimensional (spanwise-uniform) vortex structures were emitted from the separated shear layer, then they convected in the downstream direction with amplifying three-dimensional fluctuations. It is noteworthy that in the SJ cavity, three-dimensional structures are suppressed in the $F^+ = 30$ case (Figure A1e) due to the smaller amplitude of the oscillation of the cavity bottom. Therefore, two-dimensional vortex structures more clearly emerge in the vicinity of the leading edge, which is close to the PA actuation in Figure A1f.

Figure A2 shows the periodic and turbulent components of the Reynolds shear stress in the cases of $C_\mu = 2.0 \times 10^{-3}$ and $F^+ = 10$. The turbulent component is dominant over the suction side in both SJ and PA, while the periodic component is stronger in the PA than in the SJ. This observation is the same in the lower frequency cases of Figure 17 for $F^+ = 1.0$ and 6.0 . It should be also noted that as in the lower frequency cases, the PA induces a stronger two-dimensional structure than the SJ, and thus the turbulent component is again locally amplified near the trailing edge ($x/c_h \simeq 0.7$), which is not observed in the SJ case.

Figure A3 shows the phase history of the decomposed Reynolds shear stress in the cases of $C_\mu = 2.0 \times 10^{-3}$ and $F^+ = 10$. As was shown in Figures 18 and 19, the turbulent component mainly contributes to the exchange of the chordwise momentum in both SJ and PA cases. Moreover, the coherent vortex structures and periodic component of the Reynolds shear stress are stronger in the PA than in the SJ, which are also similar to the lower frequency cases of $F^+ = 1.0$ and 6.0 .

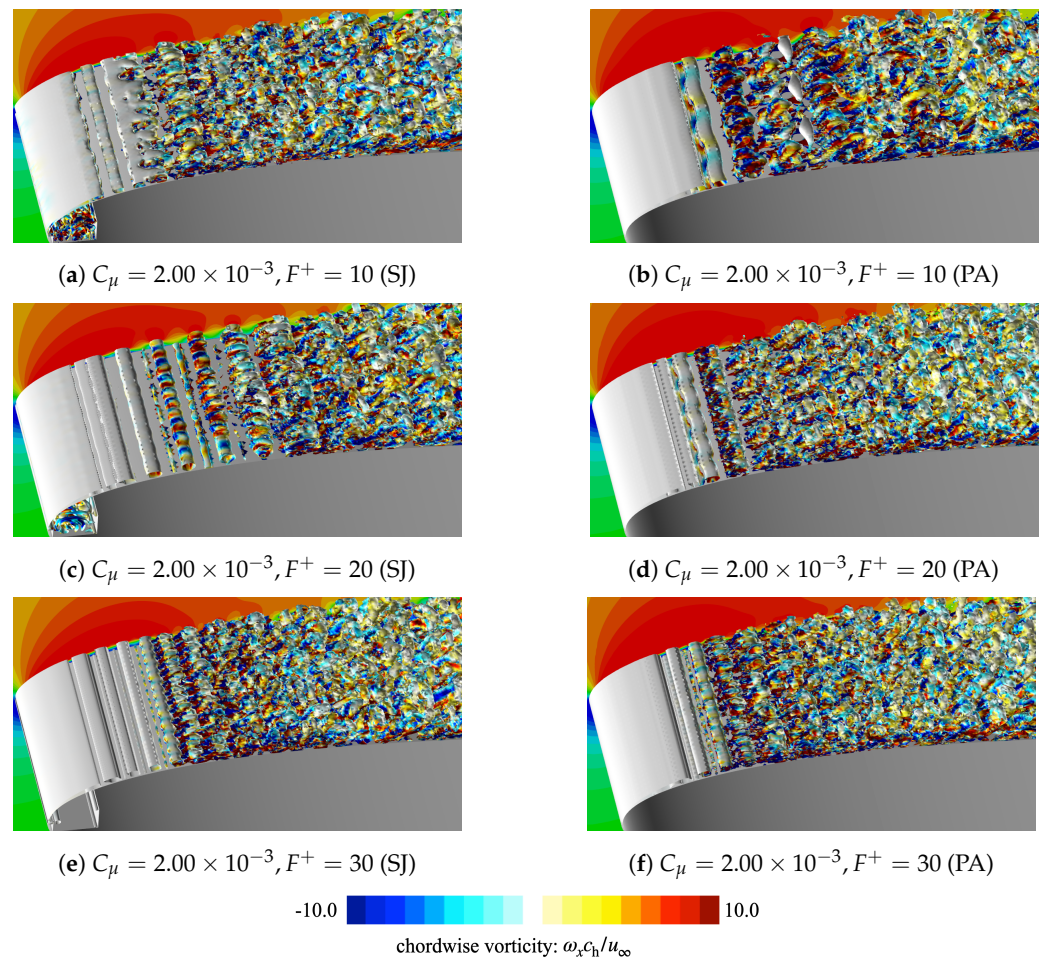


Figure A1. Instantaneous vortex structures around the leading edge. Isosurfaces show the second invariant of the velocity gradient tensor (colored by chordwise velocity u/u_∞ for 0.0 to 1.5).

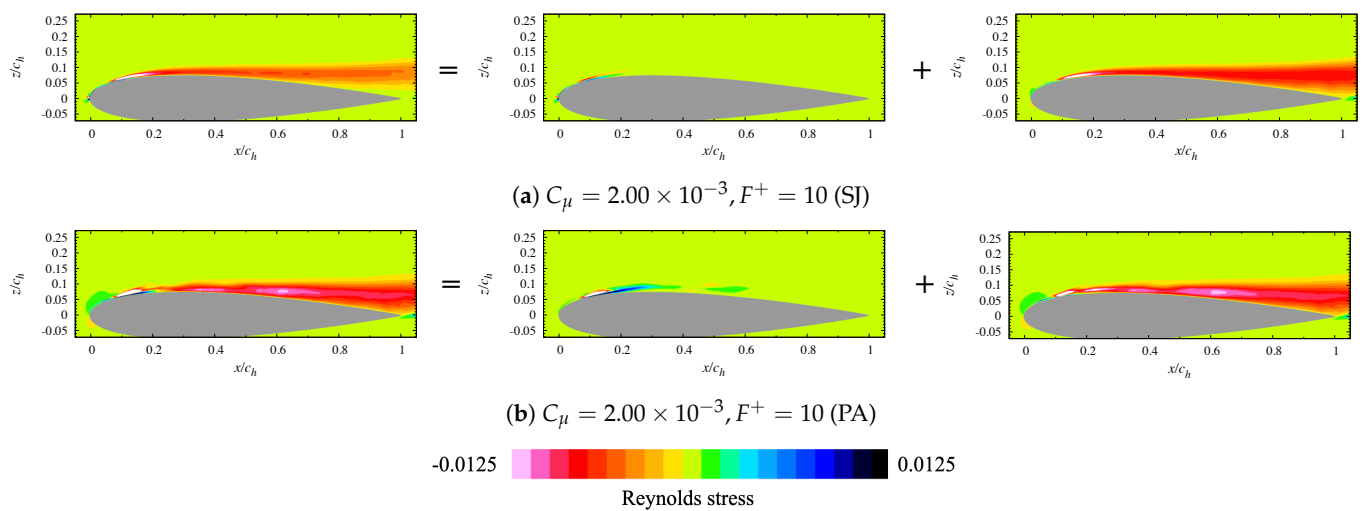


Figure A2. Phase decomposition of the Reynolds shear stress $-\overline{u'w'}/u_\infty^2$. The Reynolds shear stress is decomposed into periodic ($\overline{u\tilde{w}}$) and turbulent ($\overline{u''w''}$) components.

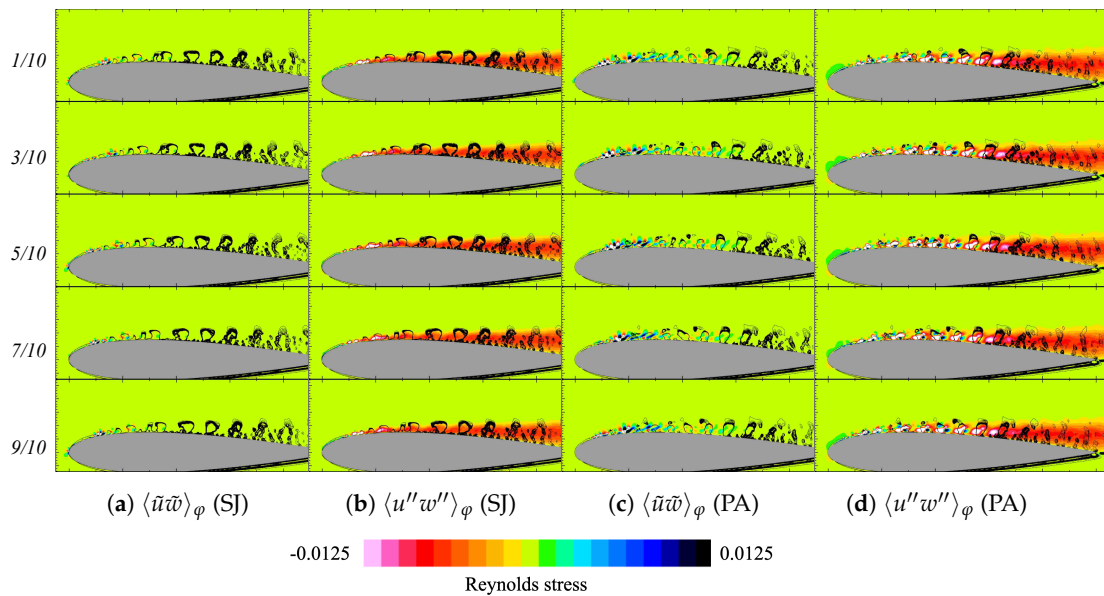


Figure A3. Phase decomposition of the Reynolds shear stress in the case of $C_\mu = 2.0 \times 10^{-3}$, $F^+ = 10$. Contour color shows periodic $\langle \tilde{u}\tilde{w} \rangle_\varphi$ and turbulent $\langle u''w'' \rangle_\varphi$ components. Black contours show the second invariant of the velocity gradient tensor in the phase- and spanwise-averaged flow field.

References

- Greenblatt, D.; Wygnanski, I.J. The control of flow separation by periodic excitation. *Prog. Aerosp. Sci.* **2000**, *36*, 487–545. [\[CrossRef\]](#)
- Cattafesta, L.N., III; Sheplak, M. Actuators for active flow control. *Annu. Rev. Fluid Mech.* **2011**, *43*, 247–272. [\[CrossRef\]](#)
- Greenblatt, D.; Williams, D.R. Flow Control for Unmanned Air Vehicles. *Annu. Rev. Fluid Mech.* **2022**, *54*, 383–412. [\[CrossRef\]](#)
- Smith, B.L.; Glezer, A. The formation and evolution of synthetic jets. *Phys. Fluids* **1998**, *10*, 2281. [\[CrossRef\]](#)
- Chen, F.; Yao, C.; Beeler, G.; Bryant, R.; Fox, R. Development of synthetic jet actuators for active flow control at NASA Langley. In Proceedings of the Fluids 2000 Conference and Exhibit, Denver, CO, USA, 19–22 June 2000.
- Smith, B.L.; Glezer, A. Jet vectoring using synthetic jets. *J. Fluid Mech.* **2002**, *458*, 1–34. [\[CrossRef\]](#)
- Amitay, M.; Glezer, A. Role of Actuation Frequency in Controlled Flow Reattachment over a Stalled Airfoil. *AIAA J.* **2002**, *40*, 209–216. [\[CrossRef\]](#)
- Okada, K.; Oyama, A.; Fujii, K.; Miyaji, K. Computational Study of Effects of Nondimensional Parameters on Synthetic Jets. *Trans. Jpn. Soc. Aeronaut. Space Sci.* **2012**, *55*, 1–11. [\[CrossRef\]](#)
- Zhang, W.; Samtaney, R. A direct numerical simulation investigation of the synthetic jet frequency effects on separation control of low-Re flow past an airfoil. *Phys. Fluids* **2015**, *27*, 055101. [\[CrossRef\]](#)
- Abe, Y.; Nonomura, T.; Fujii, K. Flow instability and momentum exchange in separation control by a synthetic jet. *Phys. Fluids* **2023**, *35*, 065114.
- Corke, T.; Post, M.; Orlov, D. Single dielectric barrier discharge plasma enhanced aerodynamics: Physics, modeling and applications. *Exp. Fluids* **2009**, *46*, 1–26. [\[CrossRef\]](#)
- Corke, T.C.; Enloe, C.L.; Wilkinson, S.P. Dielectric Barrier Discharge Plasma Actuators for Flow Control. *Annu. Rev. Fluid Mech.* **2010**, *42*, 505–529. [\[CrossRef\]](#)
- Sato, M.; Nonomura, T.; Okada, K.; Asada, K.; Aono, H.; Yakeno, A.; Abe, Y.; Fujii, K. Mechanisms for Laminar Separated-Flow Control using DBD Plasma Actuator at Low Reynolds Number. *Phys. Fluids* **2015**, *27*, 117101. [\[CrossRef\]](#)
- Pescini, E.; Marra, F.; De Giorgi, M.G.; Francioso, L.; Ficarella, A. Investigation of the boundary layer characteristics for assessing the DBD plasma actuator control of the separated flow at low Reynolds numbers. *Exp. Therm. Fluid Sci.* **2017**, *81*, 482–498. [\[CrossRef\]](#)
- Sato, M.; Okada, K.; Asada, K.; Aono, H.; Nonomura, T.; Fujii, K. Unified mechanisms for separation control around airfoil using plasma actuator with burst actuation over Reynolds number range of 10^3 – 10^6 . *Phys. Fluids* **2020**, *32*, 025102. [\[CrossRef\]](#)
- Yarusevych, S.; Kotsonis, M. Effect of Local DBD Plasma Actuation on Transition in a Laminar Separation Bubble. *Flow Turbul. Combust.* **2017**, *98*, 195–216. [\[CrossRef\]](#)
- Ziadé, P.; Feerob, M.A.; Sullivan, P.E. A numerical study on the influence of cavity shape on synthetic jet performance. *Int. J. Heat Fluid Flow* **2018**, *74*, 187–197. [\[CrossRef\]](#)
- Kral, L.D.; Donovan, J.F.; Cain, A.B.; Cary, A.W. Numerical simulation of synthetic jet actuators. In Proceedings of the 4th Shear Flow Control Conference, Snowmass Village, CO, USA, 29 June–2 July 1997.

19. Smith, B.L.; Glezer, A. Vectoring and small-scale motions effected in free shear flows using synthetic jet actuators. In Proceedings of the 35th Aerospace Sciences Meeting and Exhibit, Reno, NV, USA, 6–9 January 1997.
20. Yoshioka, S.; Obi, S.; Masuda, S. Turbulence Statistics of periodically perturbed separated flow over backward-facing step. *Int. J. Heat Fluid Flow* **2001**, *22*, 393–401. [[CrossRef](#)]
21. Feero, M.A.; Goodfellow, S.D.; Lavoie, P.; Sullivan, P.E. Flow Reattachment Using Synthetic Jet Actuation on a Low-Reynolds-Number Airfoil. *AIAA J.* **2015**, *53*, 2005–2014. [[CrossRef](#)]
22. Visbal, M.R. Numerical Exploration of Flow Control for Delay of Dynamic Stall on a Pitching Airfoil. In Proceedings of the 32nd AIAA Applied Aerodynamics Conference, Atlanta, GA, USA, 16–20 June 2014.
23. Lilley, A.J.; Roy, S.; Visbal, M.R. On the effect of high-frequency plasma actuator forcing for prevention of dynamic stall. In Proceedings of the AIAA SCITECH 2023 Forum, National Harbor, MD, USA, 23–27 January 2023.
24. Asada, K.; Ninomiya, Y.; Oyama, A.; Fujii, K. Airfoil Flow Experiment on the Duty Cycle of DBD Plasma Actuator. In Proceedings of the 47th AIAA Aerospace Sciences Meeting including The New Horizons Forum and Aerospace Exposition, Orlando, FL, USA, 5–8 January 2009.
25. Yarusevych, S.; Kotsonis, M. Steady and transient response of a laminar separation bubble to controlled disturbances. *J. Fluid Mech.* **2017**, *813*, 955–990. [[CrossRef](#)]
26. Kurelek, J.W.; Yarusevych, S.; Kotsonis, M. Vortex merging in a laminar separation bubble under natural and forced conditions. *Phys. Rev. Fluids* **2019**, *4*, 063903. [[CrossRef](#)]
27. Marxen, O.; Kotapati, R.B.; Mittal, R.; Zaki, T. Stability analysis of separated flows subject to control by zero-net-mass-flux jet. *Phys. Fluids* **2015**, *27*, 68–89. [[CrossRef](#)]
28. Lambert, A.; Yarusevych, S. Effect of angle of attack on vortex dynamics in laminar separation bubbles. *Phys. Fluids* **2019**, *31*, 064105. [[CrossRef](#)]
29. Sekimoto, S.; Fujii, K.; Anyoji, M.; Miyakawa, Y.; Ito, S.; Shimomura, S.; Nishida, H.; Nonomura, T.; Matsuno, T. Flow Control around NACA0015 Airfoil Using a Dielectric Barrier Discharge Plasma Actuator over a Wide Range of the Reynolds Number. *Actuators* **2023**, *12*, 43. [[CrossRef](#)]
30. You, D.; Moin, P. Active control of flow separation over an airfoil using synthetic jets. *J. Fluids Struct.* **2008**, *24*, 1349–1357. [[CrossRef](#)]
31. Benton, S.I.; Visbal, M.R. Extending the Reynolds Number Range of High-Frequency Control of Dynamic Stall. *AIAA J.* **2019**, *57*, 2676–2681. [[CrossRef](#)]
32. Aono, H.; Sekimoto, S.; Sato, M.; Yakeno, A.; Nonomura, T.; Fujii, K. Computational and experimental analysis of flow structures induced by a plasma actuator with burst modulations in quiescent air. *Mech. Eng. J.* **2015**, *2*, 15-00233. [[CrossRef](#)]
33. Suzen, Y.B.; Huang, P.G.; Jacob, J.D.; Ashpis, D.E. Numerical Simulations of Plasma Based Flow Control Application. In Proceedings of the 35th AIAA Fluid Dynamics Conference and Exhibit, Toronto, ON, Canada, 6–9 June 2005.
34. Lilley, A.; Roy, S.; Michels, L.; Roy, S. Performance recovery of plasma actuators in wet conditions. *J. Phys. Appl. Phys.* **2022**, *55*, 155201. [[CrossRef](#)]
35. Tanaka, M.; Kubo, N.; Kawabata, H. Plasma actuation for leading edge separation control on 300-kW rotor blades with chord length around 1 m at a Reynolds number around 1.6×10^6 . *J. Phys. Conf. Ser.* **2020**, *1618*, 052013. [[CrossRef](#)]
36. Wicks, M.; Thomas, F. Effect of Relative Humidity on Dielectric Barrier Discharge Plasma Actuator Body Force. *AIAA J.* **2015**, *53*, 2801–2805. [[CrossRef](#)]
37. Avino, F.; Howling, A.A.; Allmen, M.V.; Waskow, A.; Ibba, L.; Han, J.; Furno, I. Surface DBD degradation in humid air, and a hybrid surface-volume DBD for robust plasma operation at high humidity. *J. Phys. D Appl. Phys.* **2023**, *56*, 345201. [[CrossRef](#)]
38. Weigel, P.; Schuller, M.; Gratijs, A.; Lipowski, M.; ter Meer, T.; Bardet, M. Design of a synthetic jet actuator for flow separation control. *CEAS Aeronaut. J.* **2020**, *11*, 813–821. [[CrossRef](#)]
39. Fujii, K.; Endo, H.; Yasuhara, M. *Activities of Computational Fluid Dynamics in Japan: Compressible Flow Simulations, High Performance Computing Research and Practice in Japan*; John Wiley & Sons: Hoboken, NJ, USA, 1990.
40. Date, S.; Abe, Y.; Okabe, T. Effects of fiber properties on aerodynamic performance and structural sizing of composite aircraft wings. *Aerosp. Sci. Technol.* **2023**, *124*, 107565. [[CrossRef](#)]
41. Lele, S.K. Compact Finite Difference Schemes with Spectral-like Resolution. *J. Comput. Phys.* **1992**, *103*, 16–42. [[CrossRef](#)]
42. Abe, Y.; Iizuka, N.; Nonomura, T.; Fujii, K. Conservative metric evaluation for high-order finite difference schemes with the GCL identities on moving and deforming grids. *J. Comput. Phys.* **2013**, *232*, 14–21. [[CrossRef](#)]
43. Abe, Y.; Iizuka, N.; Nonomura, T.; Fujii, K. Geometric interpretations and spatial symmetry property of metrics in the conservative form for high-order finite-difference schemes on moving and deforming grids. *J. Comput. Phys.* **2014**, *260*, 163–203. [[CrossRef](#)]
44. Gaitonde, D.V.; Visbal, M.R. Padé-Type Higher-Order Boundary Filters for the Navier-Stokes Equations. *AIAA J.* **2000**, *38*, 2103–2112. [[CrossRef](#)]
45. Visbal, M.R.; Rizzetta, D.P. Large-eddy Simulation on General Geometries Using Compact Differencing and Filtering Schemes. In Proceedings of the 40th AIAA Aerospace Sciences Meeting & Exhibit, Reno, NV, USA, 14–17 January 2002.
46. Visbal, M.R.; Morgan, P.E.; Rizzetta, D.P. An Implicit LES Approach Based on High-Order Compact Differencing and Filtering Schemes. In Proceedings of the 16th AIAA Computational Fluid Dynamics Conference, Orlando, FL, USA, 23–26 June 2003.
47. Fujii, K. Unified Zonal Method Based on the Fortified Solution Algorithm. *J. Comput. Phys.* **1995**, *118*, 92–108. [[CrossRef](#)]

48. Melville, R.B.; Moiton, S.A.; Rizzetta, D.P. Implementation of a fully-implicit, aeroelastic Navier-Stokes solver. In Proceedings of the 13th Computational Fluid Dynamics Conference, Snowmass Village, CO, USA, 29 June–2 July 1997.
49. Fujii, K. High-performance computing-based exploration of flow control with micro devices. *Philosophical Trans. R. Soc. A* **2014**, *372*, 20130326. [[CrossRef](#)]
50. Nishida, H.; Nonomura, T.; Abe, T. Three-dimensional simulations of discharge plasma evolution on a dielectric barrier discharge plasma actuator. *J. Appl. Phys.* **2014**, *115*, 133301. [[CrossRef](#)]
51. Benard, N.; Moreau, E. Electrical and mechanical characteristics of surface AC dielectric barrier discharge plasma actuators applied to air flow control. *Exp. Fluids* **2014**, *55*, 1846. [[CrossRef](#)]

Disclaimer/Publisher’s Note: The statements, opinions and data contained in all publications are solely those of the individual author(s) and contributor(s) and not of MDPI and/or the editor(s). MDPI and/or the editor(s) disclaim responsibility for any injury to people or property resulting from any ideas, methods, instructions or products referred to in the content.